An Investigation of the Signal-to-Noise Ratio of the Rogowski Beam Position Monitor

von

Rahul Suvarna

Masterarbeit in Physik

vorgelegt der
Fakultät für Mathematik, Informatik und Naturwissenschaften
RWTH Aachen

angefertigt am
III. Physikalisches Institut B

vorgelegt im
Januar 2023

Erstgutachter und Betreuer
Prof. Dr. Jörg Pretz
III. Physikalisches Institut B
RWTH Aachen

Zweitgutachter
Prof. Dr. Andreas Lehrach
III. Physikalisches Institut B
RWTH Aachen

ABSTRACT

Pioneering measurements of the charged particle Electric Dipole Moment were carried out at the Forschungszentrum Jülich Cooler Synchrotron (COSY) facility by the Jülich Electric Dipole Moment Investigations (JEDI) collaboration in early 2022. A prototype electrostatic ring will be designed in the coming years with better sensitivity. The prototype ring will demand a beam with close-to-ideal parameters; therefore, extremely sensitive Beam Position Monitors (BPMs) are a must-have.

The Rogowski Beam Position Monitor is a novel BPM system designed to be compact and cheap with high precision in mind. With a footprint of 0.1 m, this BPM system can be deployed in tight locations while providing resolution in the micrometre regime over a 1 s sampling period. While this BPM system has been deployed inside COSY in the past few years, a concrete study of its Signal-to-Noise Ratio (SNR) has not yet been performed. Therefore, this study is focused on painting a picture of the SNR profile of the Rogowski BPM and quantifying its performance.

ACKNOWLEDGEMENT

First, I would like to thank my mother, Vanishree Suvarna and my father, Prakash Suvarna, immensely for their continuous support and belief in me, letting me explore the world without any fears. I wouldn't be anything without them, and no words can convey my love for them. My aunt Prema Bangera deserves a special mention for encouraging me to pursue my studies abroad and being an unconditional beacon of support.

I express my deepest gratitude to Prof. Dr. Jörg Pretz, Dr. Alexander Nass, Dr. Helmut Soltner, Dr. Frank Rathmann and Dr. Thomas Sefzick. They were very supportive and always available for quick discussions and advice whenever needed.

I also express sincere appreciation to Dr. Paramita Dey and Dr. Michael Kubocz for being the figures I could look up to for advice during difficult times and also for being there since day one in Germany, not only for me but for a whole bunch of newcomers.

I am deeply indebted to Dr. Harish Shetty and Samrin Shaikh. They were the guiding lights I needed in my darkest hours, and I am fortunate to have them on my side.

I want to mention my friends Vivek, Roudy and Prashant; you made my life in Aachen easier. And last but not least, Abhijeet, Advait, Akash and Siddhant, thanks for tolerating me.

CONTENTS

CHAPTER

1

INTRODUCTION

1.1 Matter – Antimatter Asymmetry

The observable universe is composed of matter and has a glaring absence of antimatter. The exciting part about the matter-antimatter asymmetry problem is the presence of matter; since the Big Bang should have created an equal amount of matter and antimatter, total annihilation of the matter and antimatter pair is expected [1].

However, the universe exists and thus implies the presence of an excess of matter. This survival of an excess of 'matter' particles is called Baryogenesis. By taking the ratio between the difference of the number of baryons n_B and the number of antibaryons $n_{\bar{B}}$, and the number density of CMB[†] photons, we can quantify the phenomena of Baryogenesis.

$$\eta = \frac{n_B - n_{\bar{B}}}{n_\gamma}, \tag{1.1}$$

here η is the baryon asymmetry parameter, and its value is $\eta \approx 10^{-10}$ [2]. Meanwhile, the Standard Model predicts $\eta \approx 10^{-18}$ [3].

1.2 EDM Measurements

Our current understanding of the Standard Model is insufficient to explain the matter-antimatter asymmetry [4]. This asymmetry can be explained by finding additional sources of $\mathbb{CP}^{\ddagger}$-violation.

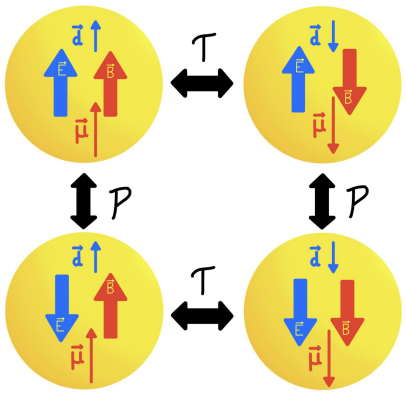

Figure 1.1: A visualization of the Parity ($\mathbb{P}$) and Time ($\mathbb{T}$) transformation [5]. Here $\vec{d}$ is the Electric Dipole Moment (EDM) and $\vec{\mu}$ is the Magnetic Dipole Moment (MDM) with $\vec{s}$ being the spin.

[†]Cosmic Microwave Background
[‡]Charge Conjugation Parity Transformation Symmetry

Violation of time reversal and parity invariance is observed in the permanent Electric Dipole Moment (EDM) of particles, which means they violate $\mathbb{CP}$ via the $\mathbb{CPT}$ theorem [6]. Therefore, EDMs are the key to understanding the mystery of the universe's origin. The MDM and EDM of a particle along the spin vector $\vec{s}$ are defined as follows:

$$\vec{\mu} = \frac{g}{2}\frac{e\hbar}{m}\vec{s} \quad \text{and} \quad \vec{d} = \frac{\chi}{2}\frac{e\hbar}{mc}\vec{s}, \tag{1.2}$$

where e is the elementary charge, m is the particle's mass, and g and χ are dimensionless scaling factors for the dipole moments. We can write the Hamiltonian of a stationary particle in an external magnetic field $\vec{B}$ and an external electric field $\vec{E}$ as

$$\mathbb{H} = -\vec{\mu}\cdot\vec{B} - \vec{d}\cdot\vec{E}. \tag{1.3}$$

Only the electric field is affected by the parity operator leaving the magnetic field and the spin untouched such that equation 1.3 becomes

$$\mathbb{P}(\mathbb{H}) = -\vec{\mu}\cdot\vec{B} + \vec{d}\cdot\vec{E}. \tag{1.4}$$

Meanwhile, the action of the time operator on equation 1.3 does not affect the electric field but flips the magnetic field and the spin, which gives

$$\mathbb{T}(\mathbb{H}) = -\vec{\mu}\cdot\vec{B} + \vec{d}\cdot\vec{E}. \tag{1.5}$$

Equations 1.4 and 1.5 clearly show that the EDM violates both $\mathbb{P}$ and $\mathbb{T}$. To measure the EDM, we need to measure its interaction with an external electric field. The electric field rotates the particle's EDM, which is either parallel or anti-parallel to the spin:

$$\frac{d\vec{s}}{dt} \propto \vec{d}\times\vec{E}. \tag{1.6}$$

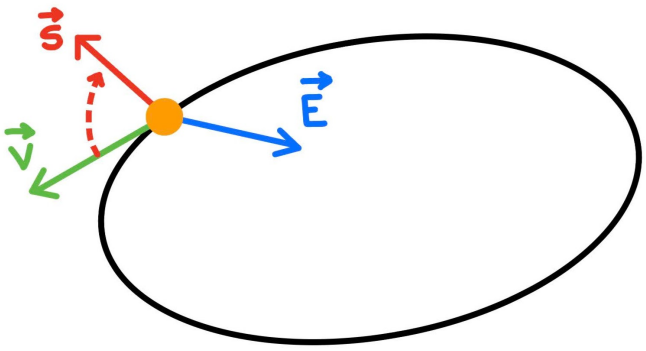

Figure 1.2: The rotation of the spin vector $\vec{s}$ around the radial axis, under the influence of a radial electric field $\vec{E}$.

Since the spin polarization is in the horizontal plane initially, the vertical rotation of the spin is used to measure the EDM. The evolution of the spin vector of a particle with velocity $\vec{v}$ under electric field $\vec{E}$ and magnetic field $\vec{B}$, including a non-vanishing electric dipole moment component, is described by the Thomas-BMT equation as follows [7]:

$$\frac{d\vec{s}}{dt} = \vec{s} \times (\vec{\Omega}_{\text{MDM}} + \vec{\Omega}_{\text{EDM}}), \tag{1.7}$$

where

$$\begin{aligned} \vec{\Omega}_{\text{MDM}} &= \frac{-e\hbar}{mc}\left[G\vec{B} + \left(G - \frac{1}{\gamma^2 - 1}\right)(c\vec{E} \times \vec{\beta})\right], \\ \vec{\Omega}_{\text{EDM}} &= \frac{-e\hbar}{mc}\left[\frac{1}{2}\chi\left((c\vec{\beta} \times \vec{B}) + \vec{E}\right)\right], \end{aligned} \tag{1.8}$$

here $G = \frac{g-2}{2}$, with g and χ as described for equation 1.2, γ is the Lorentz factor calculated for the particle with a relativistic velocity $\vec{\beta}$.

In a magnetic ring where $\vec{E} = \vec{0}$, equation 1.7 is modified as follows:

$$\frac{d\vec{s}}{dt} = \vec{s} \times \frac{-e\hbar}{mc}\left[G\vec{B} + \frac{1}{2}\chi(c\vec{\beta} \times \vec{B})\right], \tag{1.9}$$

here the magnetic field is assumed to be oriented along the vertical axis to bend the beam around the ring. An example of this case is the Cooler Synchrotron (COSY) at Forschungzentrum Jülich. The Jülich Electric Dipole moment Investigation (JEDI) Collaboration aims to perform the direct measurements of the deuteron EDM using COSY.

CHAPTER

2

COOLER SYNCHROTRON

2.1 COSY

The Cooler Synchrotron (COSY) Facility is located at Forschungszentrum Jülich in Germany. COSY is a race track-shaped synchrotron with a circumference of 184 m, with the two straight sections measuring 40 m and the two arcs measuring 52 m each. COSY can accelerate protons and deuterons up to 3.7 GeV/c momenta, corresponding to about 2.8 GeV and 2.2 GeV kinetic energy for protons and deuterons, respectively [8].

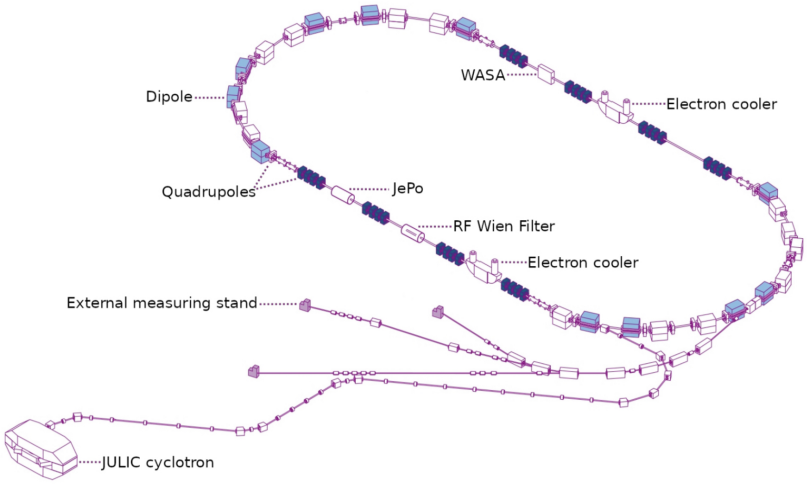

Figure 2.1: Cooler Synchrotron (COSY) accelerator at Forschungszentrum Jülich [9].

The arcs house 24 dipole magnets with a maximum field strength of 1.58 T for bending the beam. 52 quadrupole magnets for focusing and sextupole magnets for chromaticity (beam dispersion) corrections. The main features of COSY, being its 2 beam cooling systems, namely the electron cooler and the stochastic cooler, help reduce beam emittance [8].

2.2 Beam Position Monitor

Beam diagnostics is one of the most important aspects of running any accelerator or storage ring facility. The health of the beam is paramount to ensure a smooth operation. Various beam parameters, such as intensity and position, need constant monitoring.

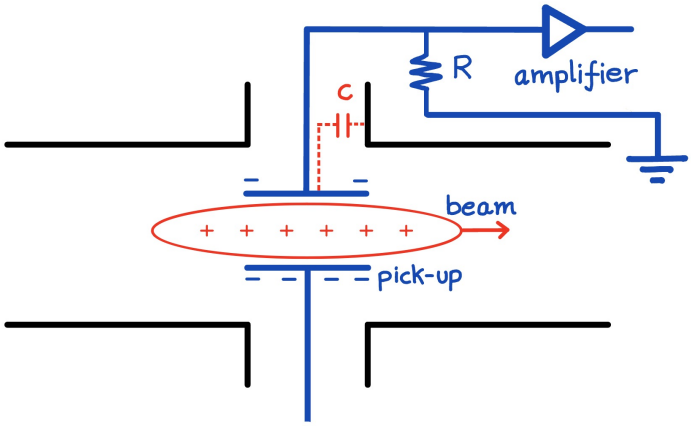

Figure 2.2: General schematic of a pick-up electrode used in capacitive beam position monitors [10] [11].

Beam Position Monitors are non-destructive diagnostic tools used to determine the beam position. Capacitive BPMs are the most common type of BPM. Image charge induction on the capacitive plates is the signal source, hence the name. The relation between the current I_{im} and the image charge Q_{im} for a plate with length l and area A, placed at a distance a from the beam centre [10], is

$$I_{\text{im}}(t) = \frac{dQ_{\text{im}}}{dt} = \frac{A}{2\pi a l} \cdot \frac{dQ_{\text{beam}}}{dt}. \tag{2.1}$$

For a beam with velocity β, we can write the following [10]:

$$\frac{dQ_{\text{beam}}(t)}{dt} = \frac{l}{\beta c} \cdot i\omega I_{\text{beam}}(\omega). \tag{2.2}$$

The voltage drop across the resistor R is the signal and is given by

$$U_{\text{im}}(\omega) = R \cdot I_{\text{im}}(\omega) = Z_t(\omega, \beta) \cdot I_{\text{beam}}(\omega). \tag{2.3}$$

Currently, there are 31 BPMs installed in COSY, all capacitive [12]. Most of these BPMs are diagonal cut BPMs, with either cylindrical or rectangular geometry depending on their placement within the COSY tunnel. A further 2 BPMs with unique geometry are installed within the beam pipe [9].

CHAPTER

3

ROGOWSKI BPM

3.1 Rogowski Coil

The Rogowski coil is made by winding a wire as a continuous helix around a toroidal dielectric core [13], as seen in Figure 3.1. It works on the principle of electromagnetic induction. Faraday's law of Electromagnetic Induction (Maxwell-Faraday law) states that an electric field is induced in a conductor due to a changing magnetic field around it [14],

$$\vec{\nabla} \times \vec{\mathbf{E}}(t) = -\frac{\partial \vec{\mathbf{B}}(t)}{\partial t}. \tag{3.1}$$

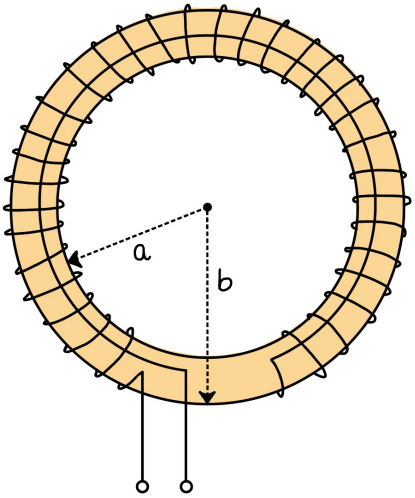

Figure 3.1: A schematic of a Rogowski coil [11].

The signal voltage induced in a Rogowski coil when placed around a conductor carrying a current I is proportional to the rate of change of the said current [13]:

$$U(t) = M \cdot \frac{dI(t)}{dt}. \tag{3.2}$$

Here M is the mutual inductance of the Rogowski coil, which itself depends on the width of the toroid W, the number of windings n, the inside and outside radii (a and b, respectively) of the toroid, and the vacuum permeability μ_0 [13]:

$$M = \mu_0 \cdot \frac{nW}{2\pi} \cdot \ln\left(\frac{b}{a}\right). \tag{3.3}$$

3.2 Making a Rogowski BPM

The Rogowski BPM is constructed using four coil segments of equal specifications, as shown in Figure 3.2. The core is made of an insulating PEEK[†] plastic, considering its features such as low cost, negligible outgassing under vacuum and ease of machining. The core body has groves for the returning quarter coil wires and small boreholes to fix them.

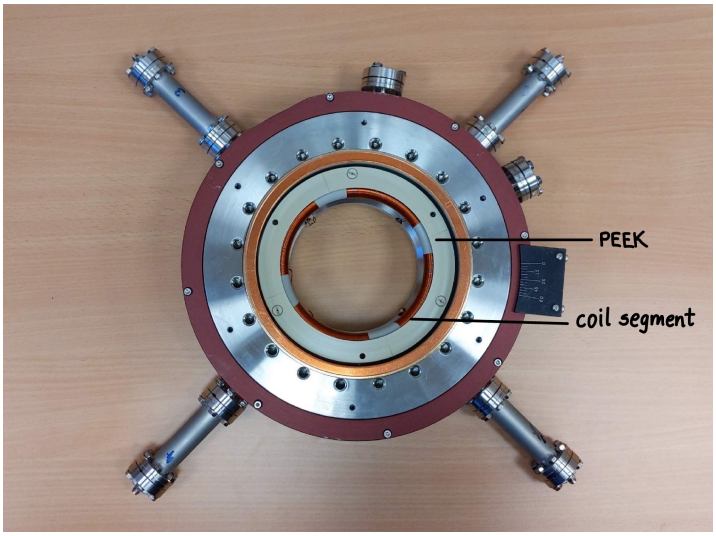

Figure 3.2: The four coil segments of the Rogowski BPM. Each segment has outputs coming out through the arms of the flange. A PEEK plastic separator is used to avoid any contact between the coils and the flange.

The relation between the magnetic flux $\Phi(t)$ and induced voltage $U(t)$ for coils with n number of windings can be written as

$$U(t) = -n\frac{\partial \Phi}{\partial t} = -n\dot{\Phi}(t). \tag{3.4}$$

The magnetic flux density generated by a current $I(t)$ is

$$\vec{B}(t) = \frac{\mu_0 I(t)}{2\pi s}\vec{e}_t, \tag{3.5}$$

with s being the radial distance from the beam centre and $\vec{e}_t$ a unit vector along the circumference.

[†]Polyether ether ketone

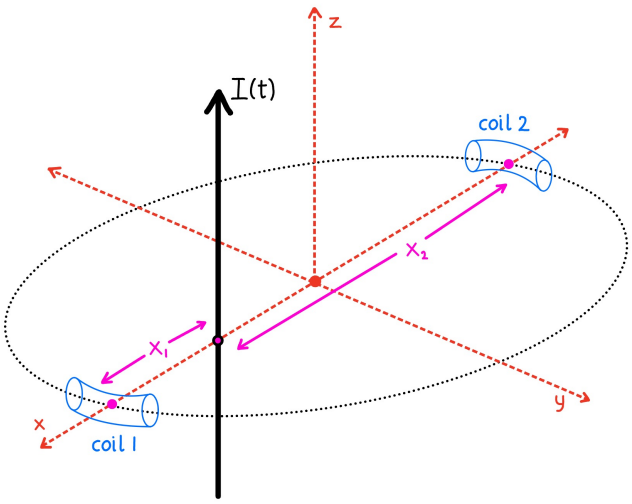

Figure 3.3: Two equivalent coils are placed diagonally opposite to each other on a circle with diameter d, such that a current-carrying conductor passes normally between them at distances x_1 and x_2 from coils 1 and 2, respectively. The distance between the centre of the circle and the conductor is $x_2 - x_1 = 2\Delta x$.

For two coils with cross-sectional area S on a circle with diameter d as seen above, the time derivative of the induced flux is given by

$$\dot{\Phi}_{1,2} = \dot{B}_{1,2} \cdot S = \frac{\mu_0 S}{2\pi} \frac{\dot{I}}{x_{1,2}}. \tag{3.6}$$

Using equation 3.4 and equation 3.6 we get...

$$U_{1,2}(t) = -n \frac{\mu_0 S}{2\pi} \frac{\dot{I}}{x_{1,2}} = \frac{\alpha}{x_{1,2}}, \tag{3.7}$$

where α is a constant defined as

$$\alpha = -n \frac{\mu_0 S \dot{I}}{2\pi}. \tag{3.8}$$

From this, the ratio of the induced voltage difference to the voltage sum in the two coils can be derived as follows:

$$\frac{\Delta U}{\Sigma U} = \frac{U_1 - U_2}{U_1 + U_2} = \frac{x_2 - x_1}{x_2 + x_1} = \frac{2\Delta x}{d}, \tag{3.9}$$

such that $2\Delta x$ is small. Each coil segment produces a voltage signal U_i which can be used to form the differential signals of two opposing sets of half coils electronically, thus allowing a simultaneous determination of the X and Y displacement of the beam. At COSY, there are currently 2 Rogowski BPM installed on either side of the RF Wien Filter. These BPMs take up less space than others, and the auxiliary equipment needed for data acquisition and processing is stored in a single compact rack.

3.3 Motivation behind Rogowski BPM

The Rogowski BPM has a tiny footprint compared to other types of BPMs, which means that multiple Rogowski BPMs can be deployed within the same space, thus improving the data precision. It is also cheaper and less time-consuming to produce owing to its simple design and a low number of distinct components. At the resonant frequency of the coil segments, the Rogowski BPMs become very precise. The resonant frequency can be tuned so that the beam frequency falls inside the resonance window of the Rogowski BPM, which is advantageous when used in a storage ring-type environment where the beam frequency is fixed.

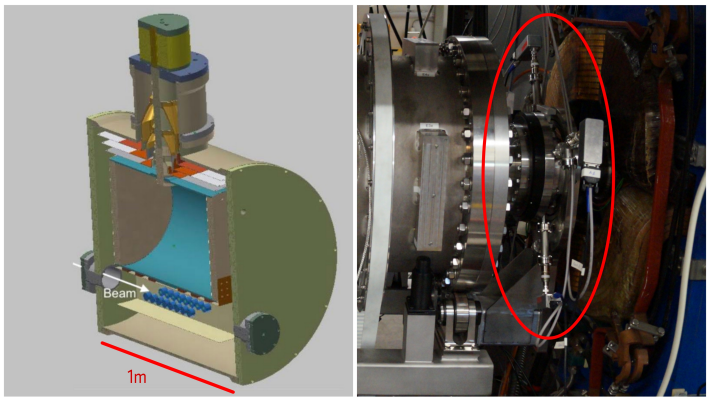

Figure 3.4: Image to the left is a schematic of the SQUID-based BPM [15]. Image to the right is one of the Rogowski BPM (highlighted by red marker) currently deployed at COSY [16].

Superconducting Quantum Interference Devices (SQUID) based BPMs have also been proposed for use in the EDM experiment. However, the SQUID-based BPMs need considerably more space ($\sim$ 1 m) [15] compared to the Rogowski BPMs ($\sim$ 0.1 m). The SQUID-based BPMs need cryogenic temperatures to operate [17], thus demanding an active cooling system. The Rogowski BPMs can be operated at room temperature, thus making them less prone to failures due to a cooling loss event. The signal-to-noise ratio serves an essential role in determining a device's effectiveness; thus, a comparative analysis of the SNR of the Rogowski BPM and the SQUID-based BPM needs to be done. In this work, an investigation is made into the SNR of the Rogowski BPM.

CHAPTER

4

NOISE

4.1 Noise

Every electronic component has an intrinsic electronic noise level. This noise level is a collective product of various effects, for example, 'Thermal Noise' [18] and 'Shot Noise' [19].

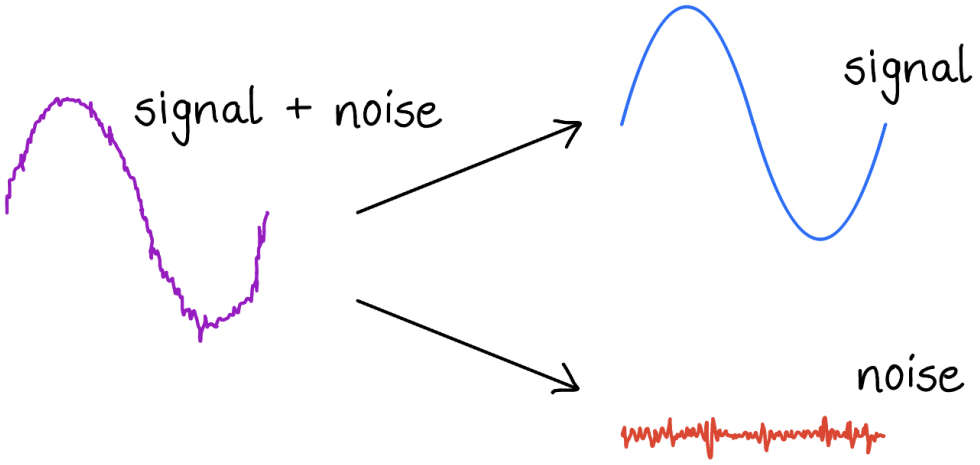

Figure 4.1: Every electronic signal consists of a pure signal component and a noise component.

Thermal noise is an electrical disturbance caused by the thermal agitation of free charges like free electrons and holes. Thermal noise is sometimes referred to as the Johnson-Nyquist noise [20].

For frequencies much smaller than $\frac{kT}{h}$ ($\approx 6\,\mathrm{THz}$ for $T = 300\,\mathrm{K}$), the thermal noise can be written as

$$U_{\text{thermal}}^{\text{noise}} = \sqrt{4k_B T R \Delta f}\,, \tag{4.1}$$

where k_B is the Boltzmann constant, T is the temperature in kelvin, R is the resistance, Δf is the bandwidth, and h is the Planck constant.

Shot noise can be attributed to the discrete nature of the charge, meaning that the final current is a sum of all the individual charge carriers. In electric circuits, there are random fluctuations in the current due to the discreteness of the electrons [20].

Shot noise is also called Schottky noise and is represented as

$$U_{\text{shot}}^{\text{noise}} = \sqrt{2qI\Delta f}\,, \tag{4.2}$$

where q is the elementary charge and I is the current.

4.2 Noise Spectral Density

If $U_{\omega}^{\text{noise}}(t)$ is the noise we aim to measure, then its component at any given frequency ω can be written as [21]

$$U_{\omega}^{\text{noise}}(t) = \sqrt{2}R\sin(\omega t + \theta), \tag{4.3}$$

with R being the root-mean-square amplitude and θ being the phase noise. These variables can also be written in the form of the *in-phase* component X and the *quadrature* component Y as [21]

$$X = YR\cos(\theta) = R\sin(\theta). \tag{4.4}$$

We can rewrite equation 4.3 as [21]

$$U_{\omega}^{\text{noise}}(t) = \sqrt{2}X\sin(\omega t) + \sqrt{2}Y\cos(\omega t). \tag{4.5}$$

The instantaneous noise power $p_{\omega}(t)$ is obtained by squaring the noise signal $U_{\omega}^{\text{noise}}(t)$, and by performing the time average over period T, we get the time-averaged noise power [21]

$$P_{\omega} = \frac{1}{T}\int_{T} p_{\omega}(t)dt = X^2 + Y^2. \tag{4.6}$$

The final noise power P_n is obtained by performing ensemble averaging (ε) of P_{ω} [21]

$$P_n = \varepsilon(X^2) + \varepsilon(Y^2). \tag{4.7}$$

The second moments are replaced by their variance since X and Y are zero-mean random variables [21] which result in

$$P_n = \sigma_X^2 + \sigma_Y^2. \tag{4.8}$$

By dividing the noise power P_n by twice the low-pass filter bandwidth B, we obtain the noise power spectral density S_n [22] and is given by

$$S_n = \frac{P_n}{2B} = \frac{1}{2}\left(\frac{\sigma_X^2}{B} + \frac{\sigma_Y^2}{B}\right) = \frac{1}{2}(S_X + S_Y). \tag{4.9}$$

where S_X and S_Y are the *in-phase* and *quadrature* component spectral densities respectively. Generally, the *in-phase* and *quadrature* components are equal, and therefore it is sufficient to measure either S_X or S_Y to determine the S_n [21]. To obtain the noise spectral density, we take the square root of the noise power spectral density S_n, i.e., $\sqrt{S_n} = \sqrt{S_X}$.

4.3 Noise Measurement using Lock-In Amplifiers

Noise measurements are carried out with the Zurich Instruments HF2LI lock-in amplifier [23] using the LabOne software [24] provided with the device. The lock-in amplifier has a sweeper function which can be used to sweep through various parameters, for example, frequency.

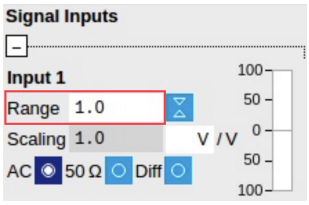

Figure 4.2: Input range set to 1 V. This is the input range used for all the experiments performed in the next chapter.

Before starting any measurement, selecting an appropriate 'Input Range' is necessary to avoid saturation [25]. Depending on the sample size, sweep precision, and a few other parameters, the measurement could take anywhere from a few minutes to several hours.

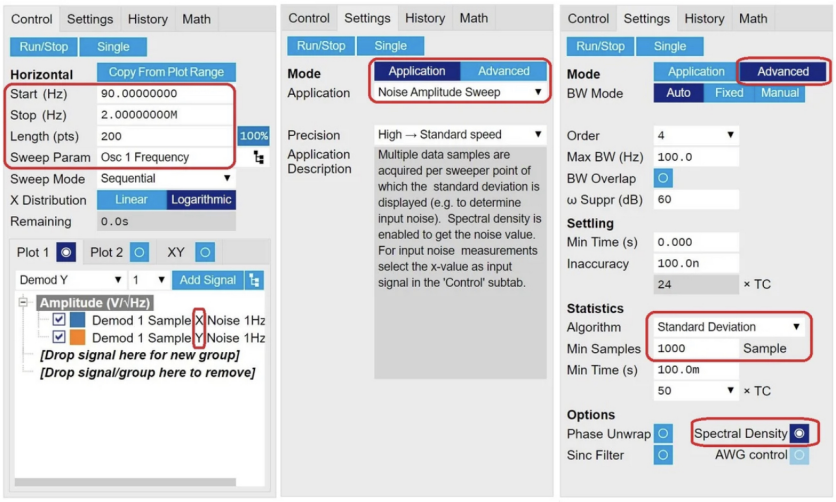

Figure 4.3: The sweeper tool dialogue box in the LabOne software [21].

The frequency range, sample size (number of points measured), and signal component to be plotted can be set as required in the 'Control' dialogue box in the sweeper tool. The sweeper tool offers a noise amplitude sweep option which takes noise data samples in the selected frequency range. To use it, open the 'Settings' tab, set the 'Application' to 'Noise Amplitude Sweeper' and select the 'Spectral Density' option. The input port should be shorted using a short cap [26].

CHAPTER

5

EXPERIMENTS

5.1 General Setup

The general setup consists of fixed wire terminated with a 50 Ω load. It is made to pass through the BPM housing, which consists of a Rogowski BPM fixed to flanges mounted on static motors. These motors facilitate the motion of the BPM setup in the X-Y plane. The movement of the BPM setup with respect to the wire is used to simulate the beam's position. Each coil segment is connected to a pre-amplifier, which then connects to one of the input ports of the lock-in amplifier via an approximately 2 m long coaxial cable.

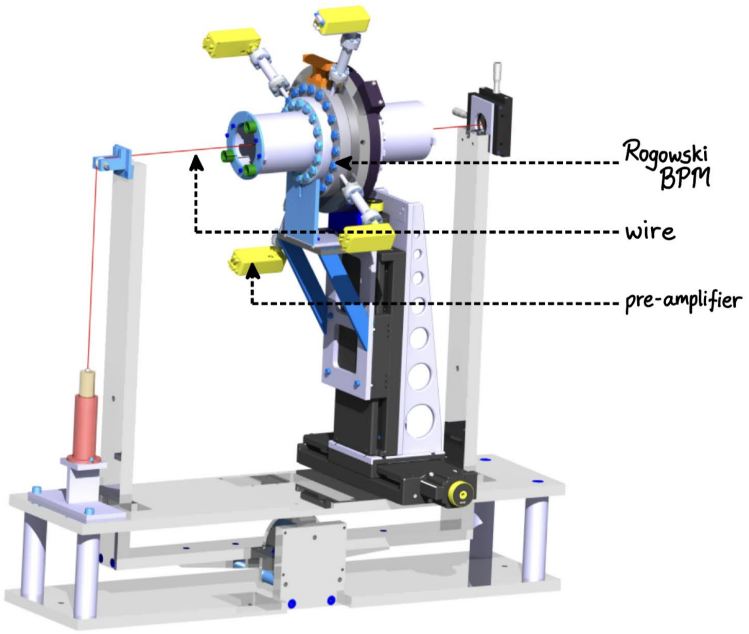

Figure 5.1: A model of the laboratory setup, wire indicated in red passing through a tube-like structure housing the BPM and pre-amplifiers in yellow.

A signal generator is used to send a sinusoidal signal through the wire, which simulates the particle beam, and another signal generator sends a square-wave signal[†] to the lock-in amplifier. These signal generators are synchronized with each other. Two lock-in amplifiers are required per BPM, as each lock-in amplifier used here has two input ports.

The setup in Figure 2.1 is a laboratory representation of the actual system inside the COSY tunnel. It thus can be used to draw ideas while designing the experiments to determine the SNR of the Rogowski BPM. The experiments that follow consider the different components from this general setup in the following order:

[†]the lock-in amplifier only accepts an external reference signal in TTL format

1. Lock-in Amplifier.
2. Cable.
3. Pre-amplifier.
4. Coil.
5. Pre-amplifier + Coil.

5.2 Noise Measurements

5.2.1 Lock-In Amplifier

The Zurich Instruments HF2 lock-in amplifiers are used as the data collection and processing hubs in the Rogowski BPM setup. The sweeper tool provided in the LabOne application is used for noise measurement. The input port of the lock-in amplifier is shorted, and measurements are carried out at various input ranges.

Figure 5.2: An image of the Zurich Instruments HF2 lock-in amplifier used in the BPM setup.

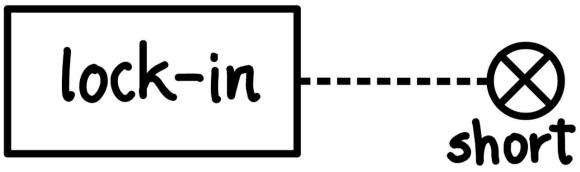

Figure 5.3: An equivalent circuit representing the setup used for the lock-in amplifier noise measurement.

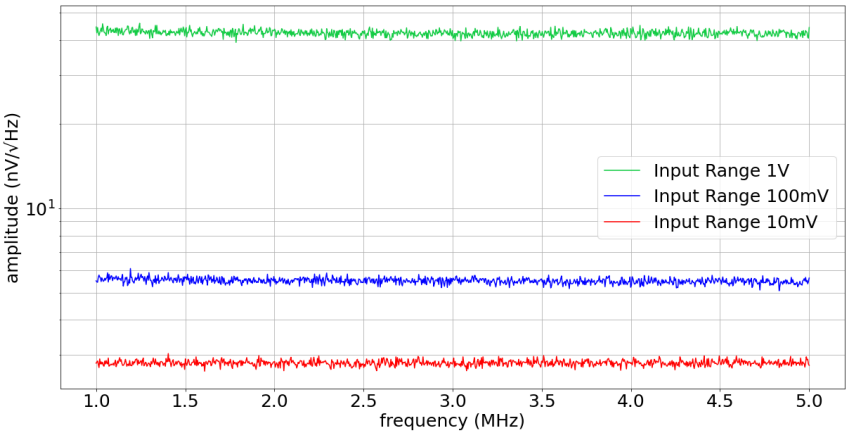

Figure 5.4: Noise characteristics of the Zurich Instruments HF2 lock-in amplifier at various input ranges

The input ranges in consideration here are 10 mV, 100 mV and 1 V. It is observed that the noise level varies with the input range of the lock-in amplifier. The larger the input range, the larger the noise floor. The noise at 10 mV input range is $\sim 3\,\mathrm{nV}/\sqrt{\mathrm{Hz}}$ and $\sim 6\,\mathrm{nV}/\sqrt{\mathrm{Hz}}$ at 100 mV.

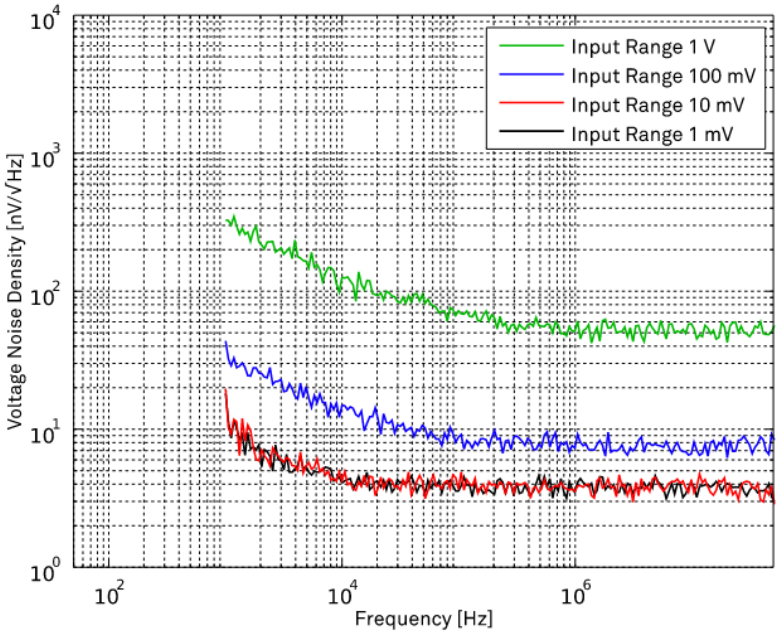

Figure 5.5: Manufacturer provided noise performance specification of the Zurich Instruments HF2 lock-in amplifier [24].

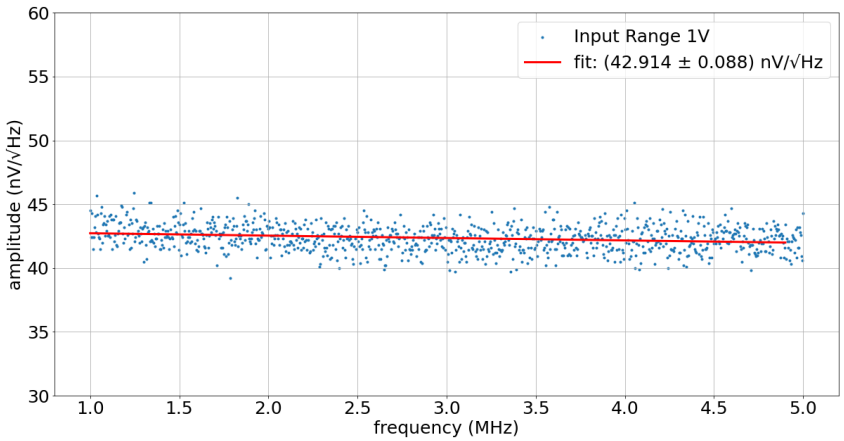

Figure 5.6: Input noise of the Zurich Instruments HF2 lock-in amplifier at 1V input range.

For the input range of 1 V, the observed noise level is (42.914±0.088) nV/$\sqrt{\text{Hz}}$. This result is in line with the manufacturer's specifications [24].

5.2.2 Cable

The second component of the Rogowski BPM setup is the coaxial cable connecting the lock-in amplifier and the pre-amplifier. For this, a 2 m long RG 58 C/U Marine coaxial cable [27], with one male BNC connector and one male SMA connector, is used. At first, an investigation is made to determine if the use of braided copper sleeves provides a performance improvement.

Figure 5.7: An image of the regular coaxial cable (left) and the shielded (with a braided copper sleeve) coaxial cable (right).

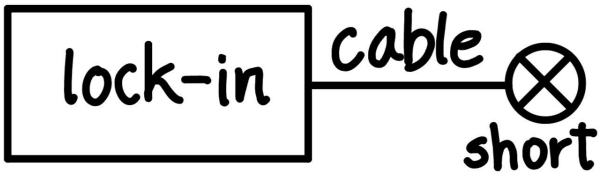

Figure 5.8: An equivalent circuit representing the setup used for the cable noise measurement.

The experimental setup consists of the cable connected to the lock-in amplifier input port. The cable is shorted using the short cap, and the measurements are performed using the sweeper tool at different input ranges (10 mV, 100 mV and 1 V). The cable is then covered using a braided copper sleeve, and the ends are taped off using PVC electrical insulating tape, exposing the connectors (see Figure 5.7). The experiment is then repeated as before.

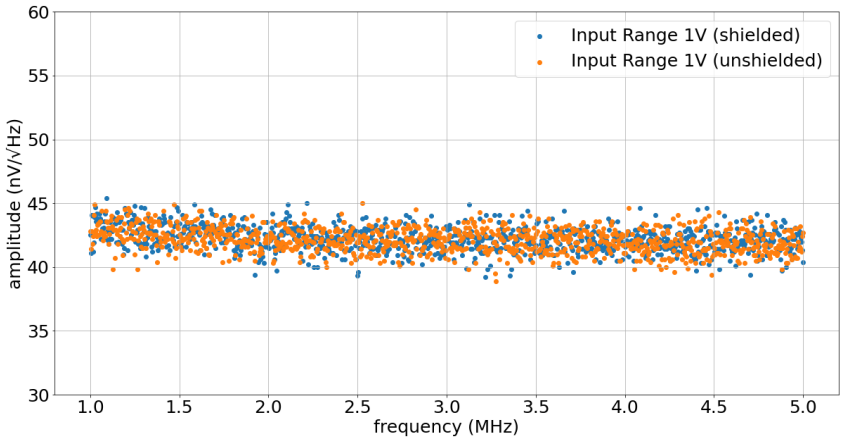

Figure 5.9: Comparison of the noise characteristics of the shielded and unshielded cable in addition to the lock-in amplifier at 1 V input range.

At 1 V range, the shielded and unshielded cables show a similar noise level of $\sim 42\,\mathrm{nV}/\sqrt{\mathrm{Hz}}$. No evidence of an improvement in the noise characteristics is observed.

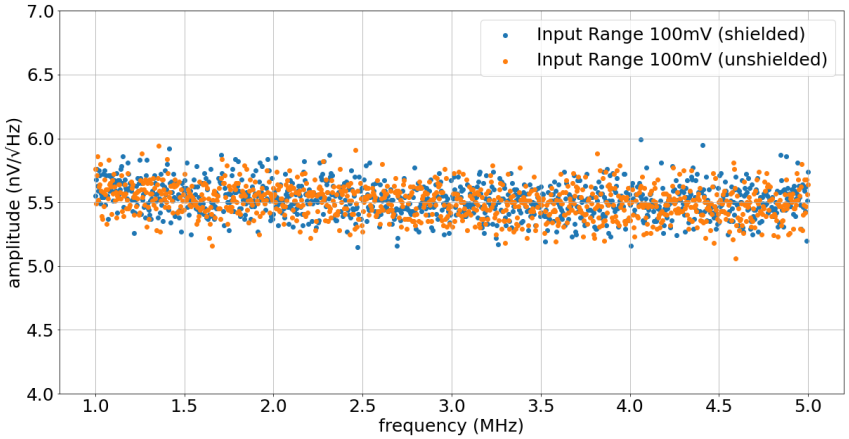

Figure 5.10: Comparison of the noise characteristics of the shielded and unshielded cable in addition to the lock-in amplifier at 100 mV input range.

At 100 mV input range, the shielded and unshielded cables show a similar noise level of $\sim 5.5\,\mathrm{nV}/\sqrt{\mathrm{Hz}}$. Noise characteristics are observed to be identical in both cases.

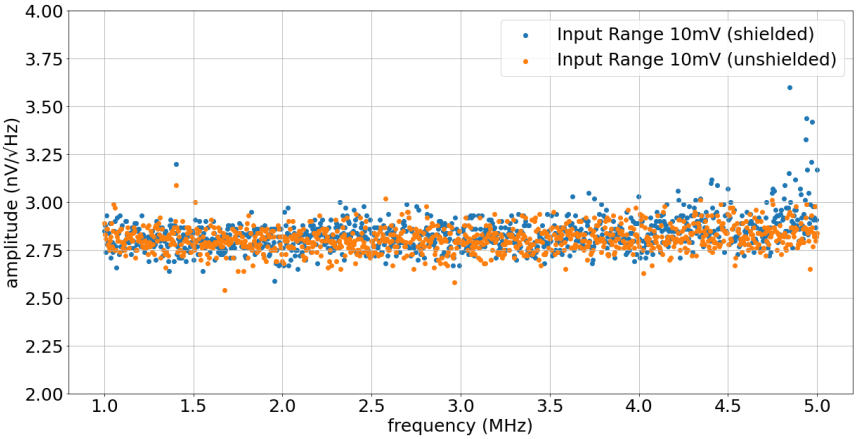

Figure 5.11: Comparison of the noise characteristics of the shielded and unshielded cable in addition to the lock-in amplifier at 10 mV input range.

When using 10 mV input range, the noise floor is observed to be at $\sim 2.8\,\mathrm{nV}/\sqrt{\mathrm{Hz}}$ for both the cables, shielded and unshielded. There is a minor variation in the results between the frequency range 4.5 to 5 MHz which can be safely ignored. It can be concluded that shielded does not influence the noise at any given input range.

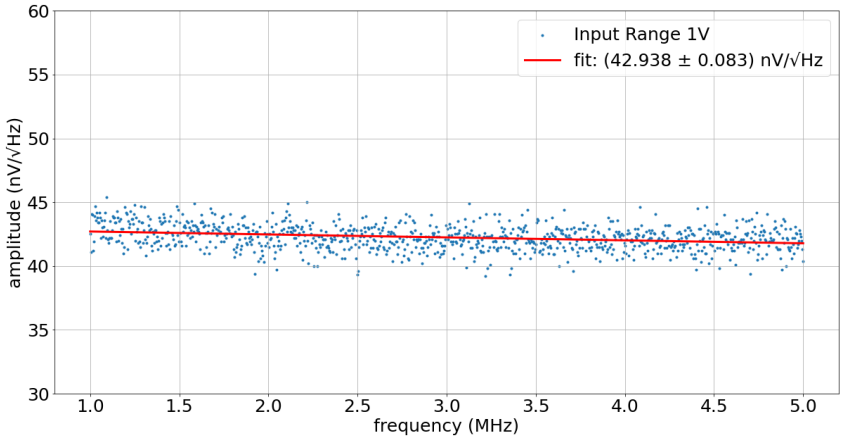

Figure 5.12: Input noise of the cable (shielded) in addition to the lock-in amplifier at 1V input range.

Using the shielded cable, the noise floor of this setup, which includes the lock-in amplifier and the cable, is $(42.938 \pm 0.083)\,\mathrm{nV}/\sqrt{\mathrm{Hz}}$. The noise contribution from the cable is thus $(1.435 \pm 0.121)\,\mathrm{nV}/\sqrt{\mathrm{Hz}}$. The cables have an attenuation value of 3 dB/100 m at 5 MHz [27], which would be insignificant for a 2 m long cable.

5.2.3 Pre-Amplifier

The signal from the coil has a low amplitude; thus, a pre-amplifier is employed before the signal is sent to the lock-in amplifier. We measure the gain for each pre-amplifier first and then measure the output noise contribution; we then determine the input noise of the pre-amplifier. For a pre-amplifier, there are two types of noise contributions, input noise and output noise. The input noise $U_{\mathrm{input}}^{\mathrm{noise}}$ and output noise $U_{\mathrm{output}}^{\mathrm{noise}}$ of a pre-amplifier with gain g are related in the following manner [28]:

$$U_{\mathrm{output}}^{\mathrm{noise}} = g \cdot U_{\mathrm{input}}^{\mathrm{noise}}. \tag{5.1}$$

Figure 5.13: The pre-amplifiers used in the BPM setup. Switches visible on the underside of the pre-amplifier to the right.

Figure 5.14: The power supply used to power the pre-amplifiers. The power supply is connected to a transformer to avoid the grounding to the mains.

5.2.3.1 Switches

The pre-amplifier has two switches (1 and 2) in the bottom which can be used to toggle between 6 dBV and 20 dBV gain settings. A small experiment was performed to study the effects of the switch positions on the pre-amplifier noise. The pre-amplifier is connected to the lock-in amplifier using the cable and terminated with the short cap. The switches are initially set to both ON, and then the noise sweep is performed using the lock-in amplifier sweeper tool, with the input range set to 1 V. This process is then repeated for the other three switch configurations, as seen in the table **??**.

Configuration	Switch 1	Switch 2	Amplification (dBV)
A	ON	ON	20
B	ON	OFF	6
C	OFF	ON	20
D	OFF	OFF	6

Table 5.1: Switch positions.

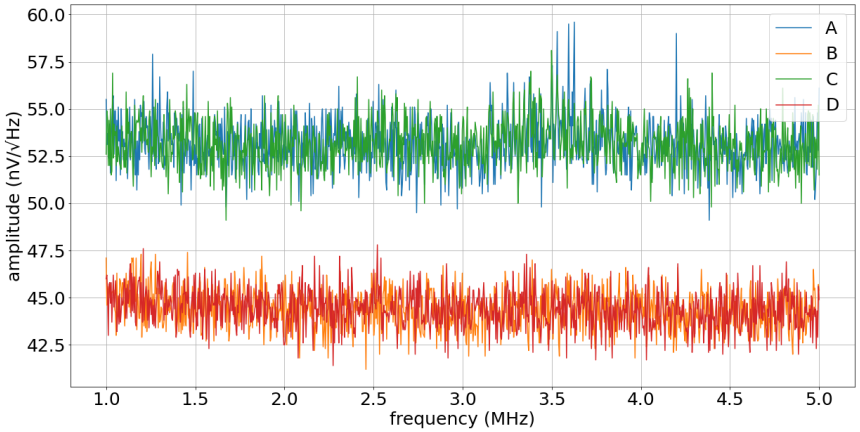

Figure 5.15: Noise characteristics of the pre-amplifier when the switches are toggled in the order as shown in the Table **??**.

The two distinct gain levels are visible in Figure 5.15, as expected [29]. From Figure 5.15, no visible effect of switch 1 on the gain of the pre-amplifier is observed. Switch 2 is responsible for toggling the gain of the pre-amplifier between the two levels mentioned above. In the previous COSY runs, where the Rogowski BPM was utilized, the pre-amplifiers were set to configuration C, i.e., switch 1 - OFF and switch 2 - ON. It can be concluded that the switch position has no effects on the noise characteristics of the pre-amplifier besides its intended purpose of gain selection.

5.2.3.2 Gain

A sinusoidal input signal of a certain amplitude (10 mV_{pp}) and frequency (1-5 MHz range) is fed to the pre-amplifier; the output of the pre-amplifier is then read out using the lock-in amplifier set to an appropriate reference frequency. An identical control sinusoidal wave (10 mV_{pp}) is then directly fed to the lock-in amplifier and read out. The gain is then calculated by taking the ratios of the amplitude of the signal from the pre-amplifier to the amplitude

of the control signal. This process is repeated for each pre-amplifier over the frequency range of interest. The pre-amplifiers have a gain of ~ 17 in the 1 to 5 MHz range.

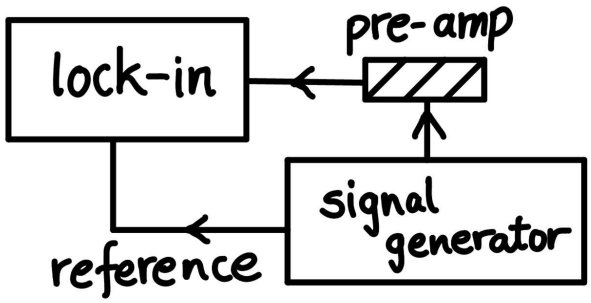

Figure 5.16: An equivalent circuit representing the setup used for the pre-amplifier gain measurement.

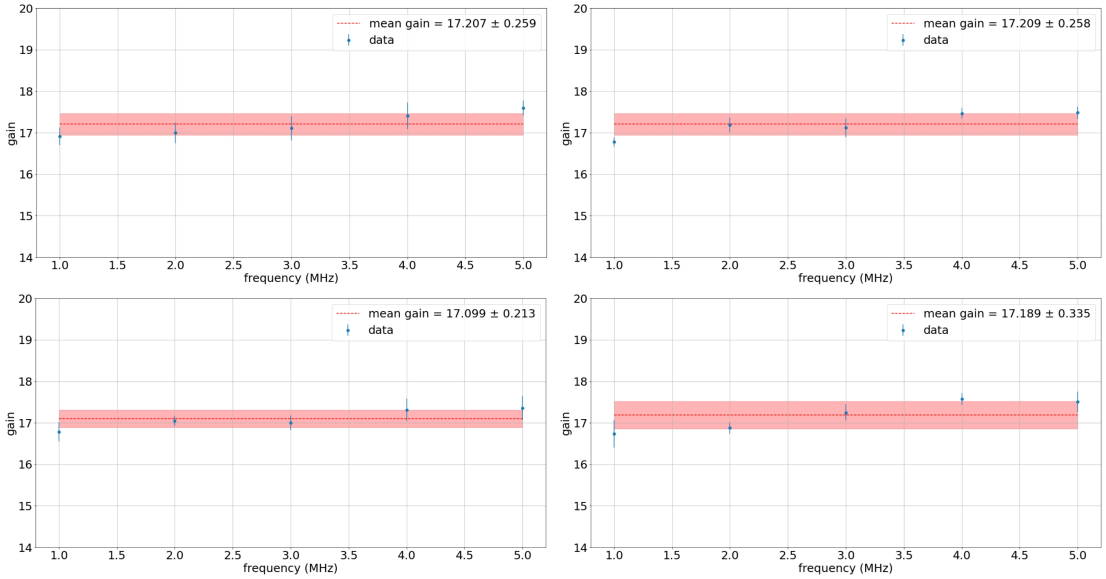

Figure 5.17: Four pre-amplifiers are used in one Rogowski BPM setup. Starting from the top-left side going clockwise (in the order 1, 2, 3 and 4), the gains of the four pre-amplifiers as a function of frequency are shown.

5.2.3.3 Noise

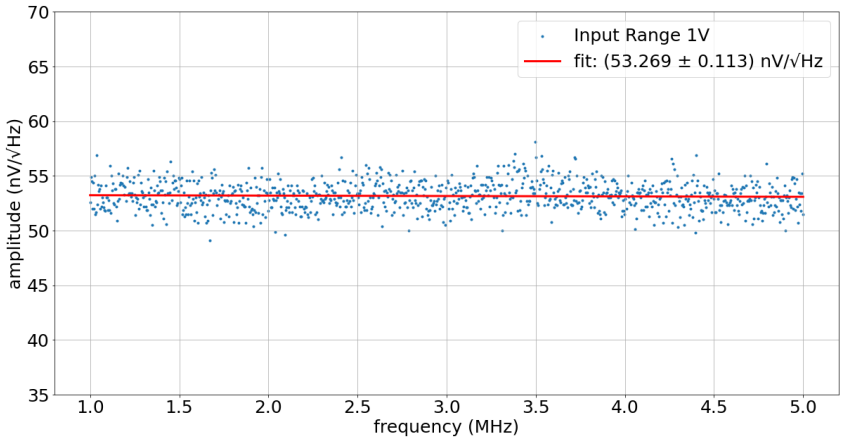

Figure 5.18: Input noise of the pre-amplifier in addition to the shielded cable and the lock-in amplifier at 1V input range.

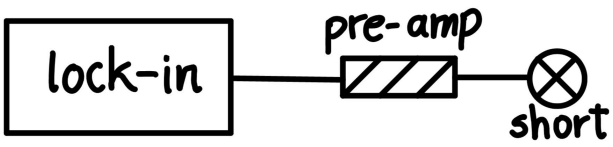

Figure 5.19: An equivalent circuit representing the setup used for the pre-amplifier noise measurement.

The output noise of the pre-amplifier is calculated from the noise measurement of the pre-amplifier in configuration C (see Table 5.1). The noise of the pre-amplifier is isolated from this measurement ((53.969 ± 0.113)-nV/$\sqrt{\text{Hz}}$) by quadratically subtracting the noise of the lock-in amplifier and the cable (see subsection 5.2.2). The output noise of the pre-amplifier is thus found to be $(31.526 \pm 0.140)\,\text{nV}/\sqrt{\text{Hz}}$. The input noise can also be extracted by substituting the gain and output noise values into equation 5.1. The input noise of the pre-amplifier is $(1.844 \pm 0.024)\,\text{nV}/\sqrt{\text{Hz}}$, which agrees with the specifications [29].

5.2.4 Coil

In this section, the noise contribution from the coil is studied. The coil noise contribution can be studied in two manners, one where the coil is isolated and one where the coil is a part of the whole BPM system; both approaches are performed here.

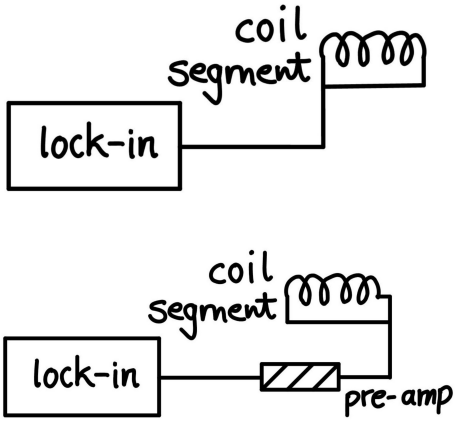

Figure 5.20: The top figure shows an equivalent circuit representing the setup used for the direct measurement of the coil noise. The bottom figure represents an equivalent circuit for the coil noise measurement setup which includes the pre-amplifier.

The most straightforward setup to perform measurements on an isolated coil is to directly connect the coil to the lock-in amplifier using a cable. The noise sweep measurements are then performed using the lock-in amplifier sweeper tool. The primary difference here is the absence of a short cap since the coil is short.

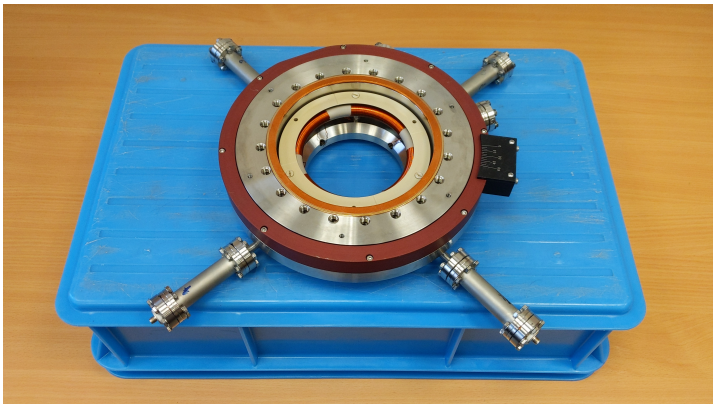

Figure 5.21: Coil setup isolated on top of a plastic crate.

The coil is connected to the lock-in amplifier via the pre-amplifier to perform measurements on the coil segment as part of the whole system. Once again, there is no need to use a short cap. In both these cases, the lock-in amplifier input range is set to 1V.

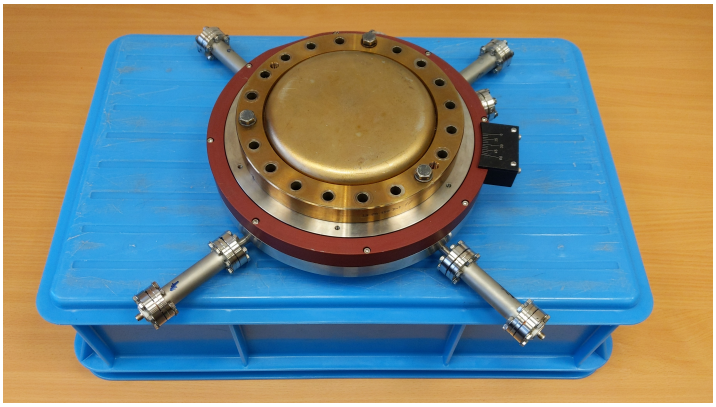

Figure 5.22: Coil setup isolated on top of a plastic crate and the ends shut using metal flanges.

An obvious source of noise error is the openings of the BPM itself. The external noise could be picked up by the coil segment under test and the other 3 segments. Therefore all tests are carried out twice, first with the coil setup open (unshielded, see Figure 5.21) and then with the coil setup ends covered by metal flanges (shielded, see Figure 5.22).

5.2.4.1 Ground Loops

The Rogowski BPM test stand, used for regular testing in previous studies [30], has a connection to the ground; in conjunction with all the other instruments used in the noise measurements, it poses a risk of introducing unwanted electromagnetic disturbances to the measurements because of ground loops [31]. The coil is therefore placed on top of a plastic crate, as seen in Figures 5.21, 5.22 and 5.23; this isolates the coil and thus provides better conditions to perform the noise measurements. The coil setup is grounded using cable (simulating the ground loops on the test stand) to verify the effectiveness of isolating the setup.

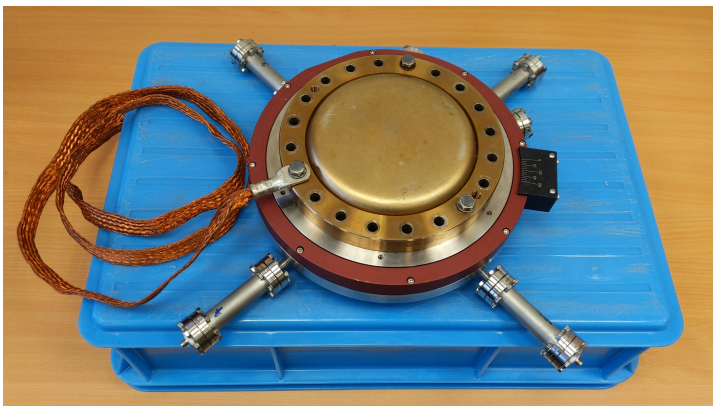

Figure 5.23: Coil setup isolated on top of a plastic crate and the ends shut using metal flanges. A grounding wire can be seen connected to the metal flange on the left side of the setup.

Figure 5.24a shows that the noise profile generally lies between 10^2 and $10^3\,\mathrm{nV}/\sqrt{\mathrm{Hz}}$, except at $\sim 1.6\,\mathrm{MHz}$, where the resonance peak is observed. At the resonant frequency, the noise is maximum at $\sim 3 \times 10^4\,\mathrm{nV}/\sqrt{\mathrm{Hz}}$. Figure 5.24b represents the coil noise profile when a pre-amplifier is used. The noise level stays between 10^3 and $10^4\,\mathrm{nV}/\sqrt{\mathrm{Hz}}$ over most of the frequency range; however, at around the resonant frequency of this setup, the noise rises to a maximum value of $\sim 9 \times 10^5\,\mathrm{nV}/\sqrt{\mathrm{Hz}}$. These plots show similar structures throughout most of the frequency range except at their respective resonant frequencies (refer section 5.3).

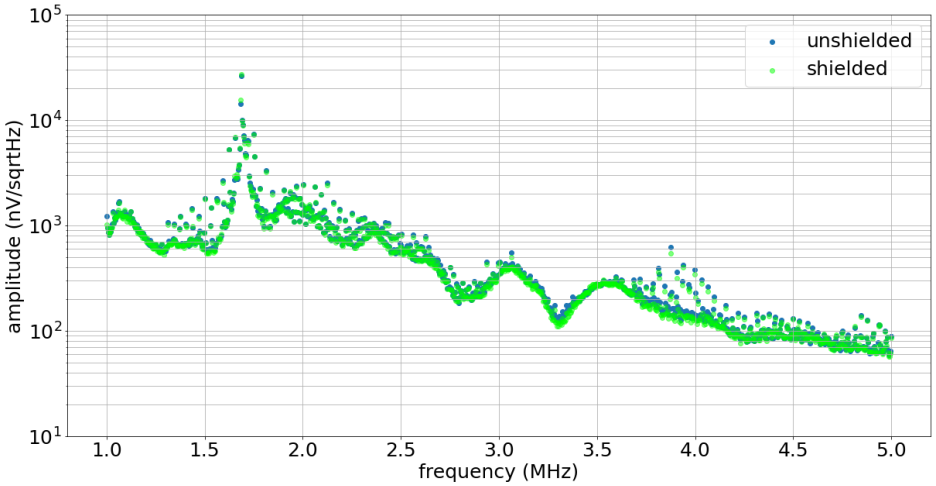

(a) Noise measurements are taken directly from the coil.

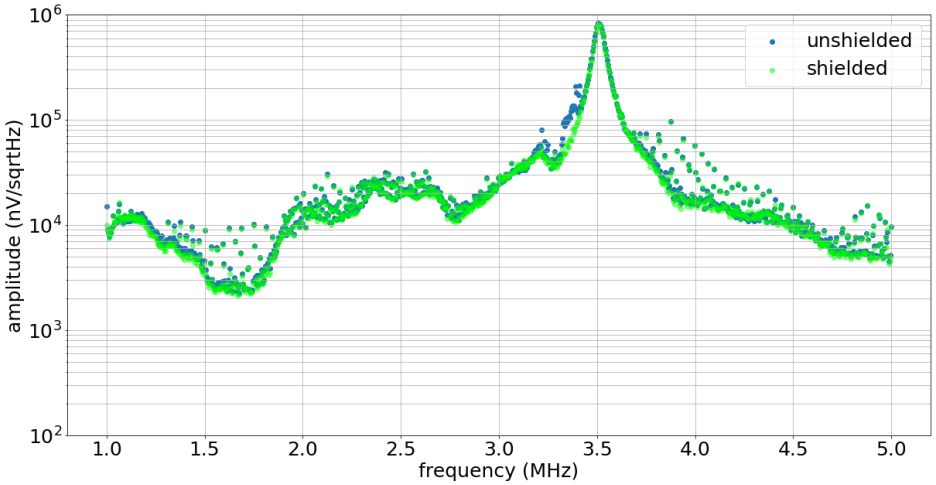

(b) Noise measurements are taken from the coil via the pre-amplifier.

Figure 5.24: A ground wire is attached to the coil setup, to simulate the ground loops when placed on the test stand (refer Figure 5.21 for the unshielded setup and Figure 5.22 for the shielded setup).

5.2.4.2 Mutual Inductance

While the measurements are being performed on one coil segment, it is necessary to ensure that the other three coil segments do not interfere since mutual inductive interference is a well-documented phenomenon in the Rogowski BPM setup [30]. This effect can be minimized by capping off the remaining three coils with 50 Ω loads.

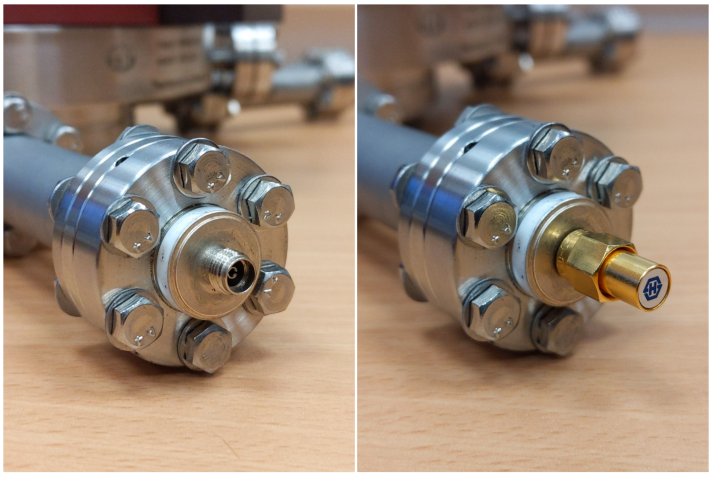

Figure 5.25: Control setup (left) has the unused coil outputs open. Capped setup (right) has unused coil outputs covered by 50 Ω load caps

A control test is performed first by taking the noise measurements of one coil segment with the unused coil segments left open, once directly and once with the pre-amplifier attached to the coil. Figure 5.26a and Figure 5.26b show the results of these experiments, respectively.

The test is repeated with the unused coil segments capped off using the 50 Ω load caps. Figure 5.27a and Figure 5.27b show the results for direct and pre-amplified coil signal tests, respectively. From Figures 5.24, 5.26 and 5.27 it is observed that the absence of the ground loops from the previous experiments shows a considerable reduction of the noise floor, regardless of the coil segments being open or capped off. However, the structures in Figure 5.27b are more tightly distributed than in Figure 5.26b. Thus, it can be concluded that capping the unused coil segments is somewhat beneficial for the noise measurements.

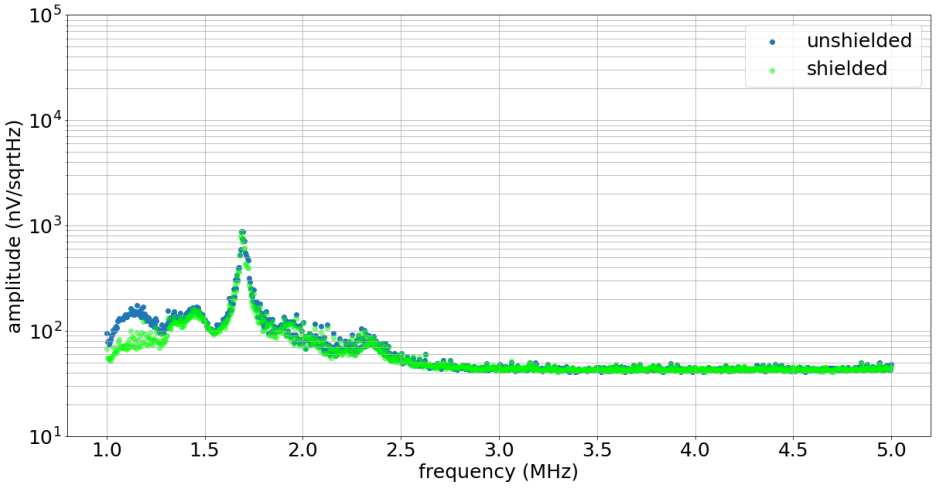

(a) Noise measurements are taken directly from the coil.

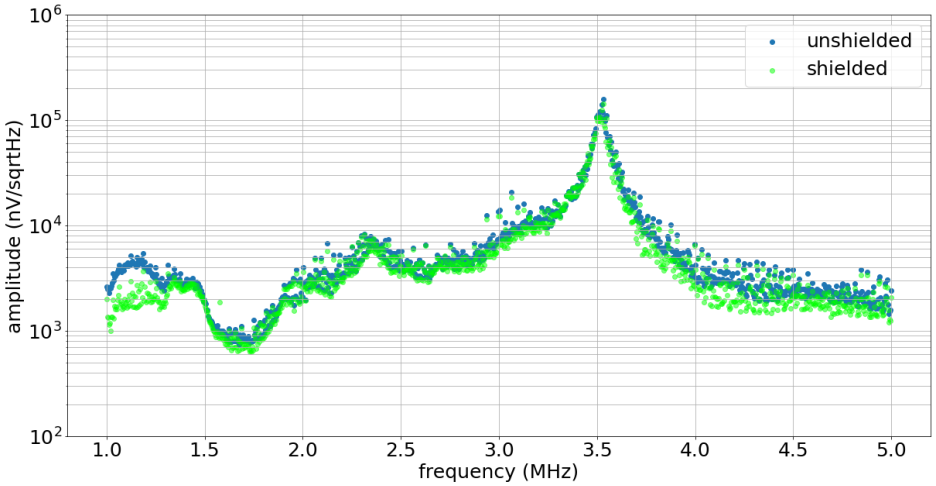

(b) Noise measurements are taken from the coil via the pre-amplifier.

Figure 5.26: Unused coil segments are left open.

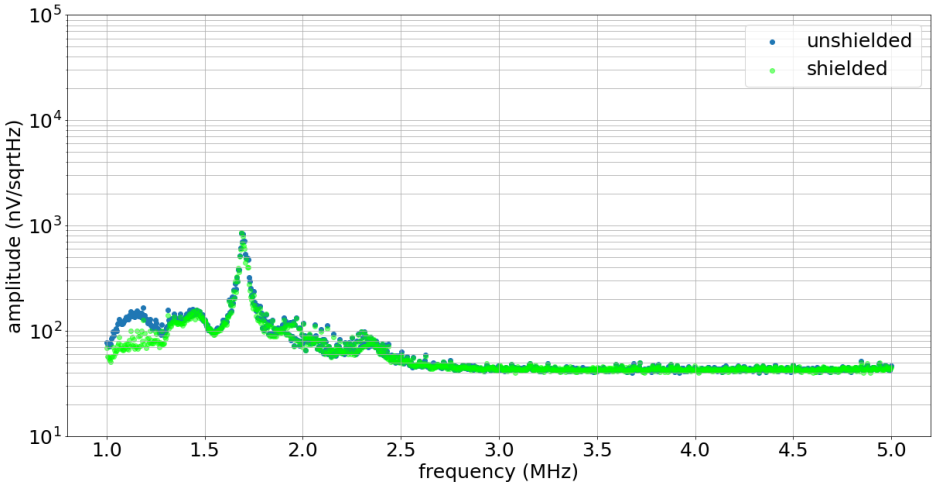

(a) Noise measurements are taken directly from the coil.

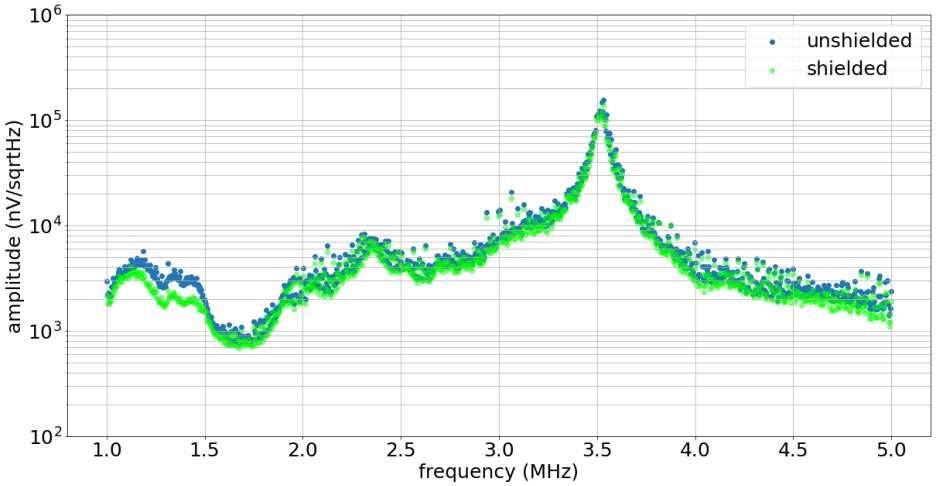

(b) Noise measurements are taken from the coil via the pre-amplifier.

Figure 5.27: 50 Ω loads used to cap coils not in use.

5.2.4.3 Pick-up

Now the question of whether the load acts as an antenna arises, which is studied by covering the three load caps with layers of electrical insulation topped with aluminium foil. In theory, the foil should act as a Faraday's cage and block out any high-frequency noise from the surrounding environment.

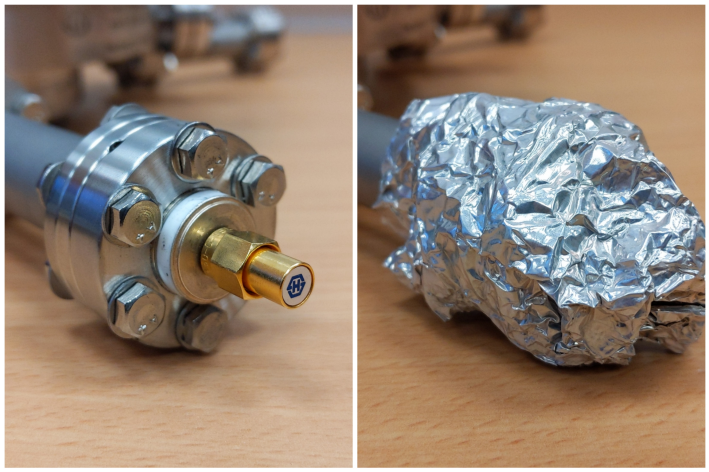

Figure 5.28: Capped setup (left) has unused coil outputs covered by 50 Ω load caps. The other setup (right), has the 50 Ω load caps on the unused coils, covered by a layer of electrical tape followed by a layer of aluminium foil.

Figure 5.29a and Figure 5.29b show that the noise distribution at the lower part of the frequency range shows unexpected behaviour. The noise in the lower half of the range is more when the coil setup is shielded. The noise level is as expected at higher frequencies. There was no apparent benefit afforded by covering the load caps with the layers of insulation tapes and aluminium foil.

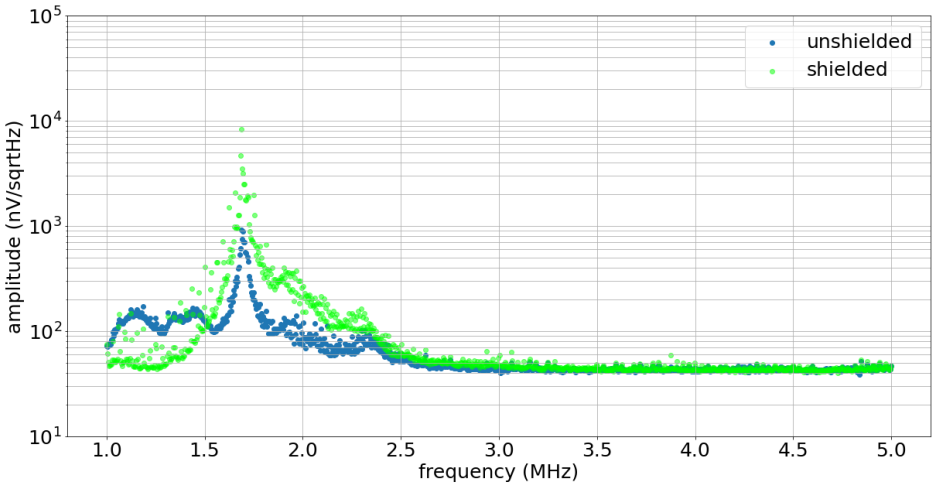

(a) Noise measurements are taken directly from the coil.

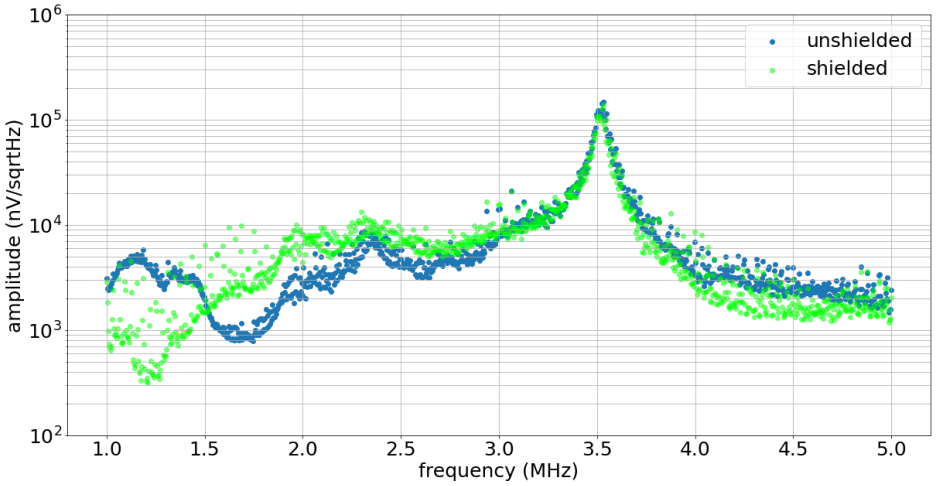

(b) Noise measurements are taken from the coil via the pre-amplifier.

Figure 5.29: Aluminium foil and electrical tape covering the 50 Ω loads used to cap coils not in use.

5.2.4.4 Best Result

From the data collected in the above experiments, it is observed that the noise profile is generally better when the coil setup is shielded, i.e., the metal flanges cover the ends. The effectiveness of isolating the coil setup on an insulated stand is also verified. Covering the unused coil segments with 50 Ω load caps is also observed to give better results (Figure 5.27).

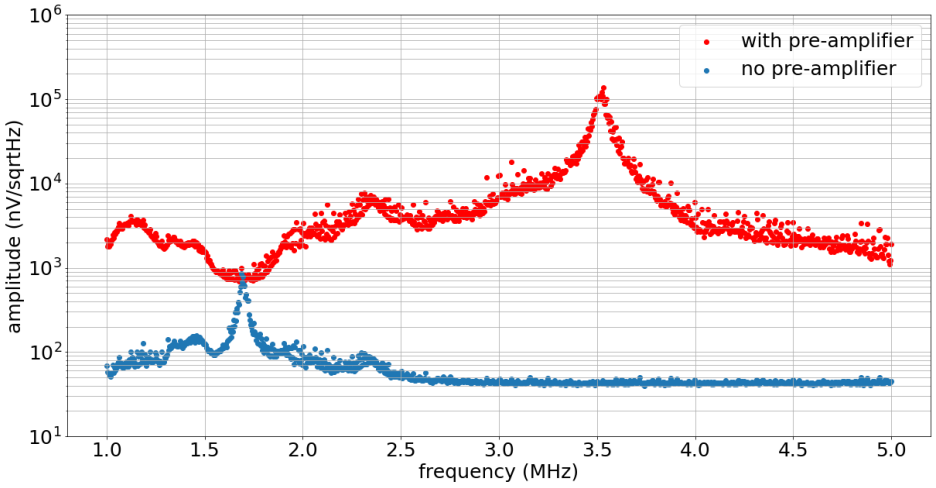

Figure 5.30: Results from the coil setup shielded with metal flanges, isolated on top of an insulated stand and unused coil segments capped off with 50 Ω load caps.

The results in Figure 5.30 were obtained by following the best practices mentioned above. The blue curve represents the direct noise measurement of the coil. It has a resonance peak at 1.689 MHz with an amplitude of $8.590 \times 10^2\,\mathrm{nV}/\sqrt{\mathrm{Hz}}$. At frequencies beyond 3 MHz, the noise floor drops down to the pre-amplifier with the cable and lock-in amplifier noise level of $\sim 50\,\mathrm{nV}/\sqrt{\mathrm{Hz}}$.

The red curve represents the coil noise measurement where the pre-amplifier is used. This curve shows a resonance peak at 3.531 MHz with an amplitude of $1.385 \times 10^5\,\mathrm{nV}/\sqrt{\mathrm{Hz}}$. The structures in this curve have corresponding structures visible in the other curve at frequencies below 3 MHz. Beyond 3 MHz, the resonance peak of the circuit used here starts to take over.

5.3 Coil Impedance Measurement

An impedance measurement was performed using the Siglent SVA 1032X spectrum and vector network analyzer (SVA) [32] to determine the coil's R, L and C values. A signal splitting box (see Figure 5.33) was commissioned to split the single output port into an input and an output port necessary for the impedance measurements of the coil using the SVA.

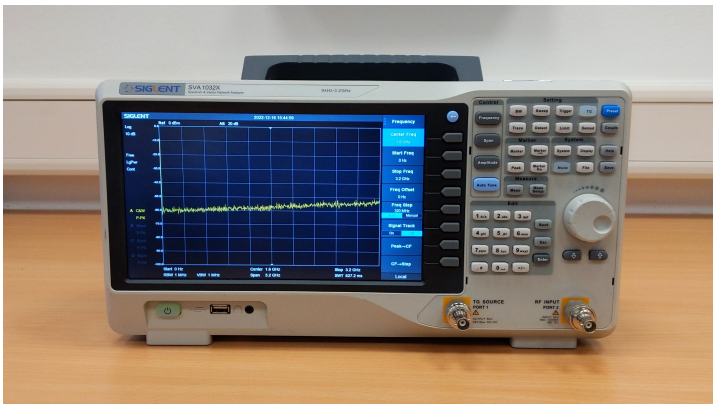

Figure 5.31: An image of the Siglent SVA 1032X spectrum and vector network analyzer used for the impedance measurement.

The SVA is set to the vector network analyzer mode and calibrated using the calibration kit to remove the resistive and capacitive influences of the cables used during the measurements. The setup is assembled as shown in Figure 5.32, and the $S21$ parameter measurement configuration is selected. The scan is performed over a preferred frequency range with the maximum number of averaging (999 sweeps over each point).

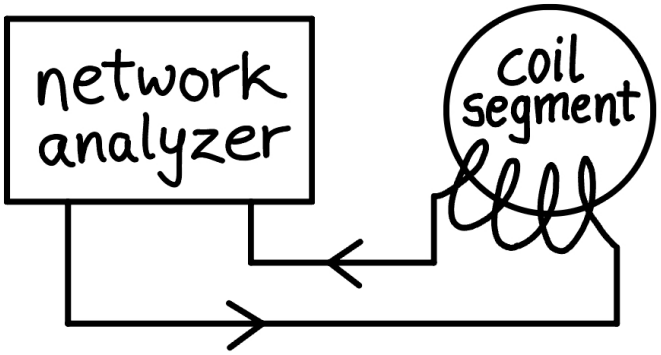

Figure 5.32: An equivalent circuit representing the setup used for the impedance measurement. The box shown in Figure 5.33 is not shown here for simplicity.

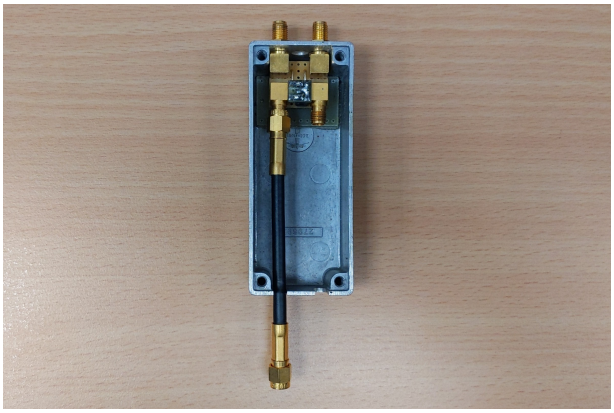

Figure 5.33: The box in this image takes one coil segment port (bottom) and splits it in to two port for the SVA input and output (top).

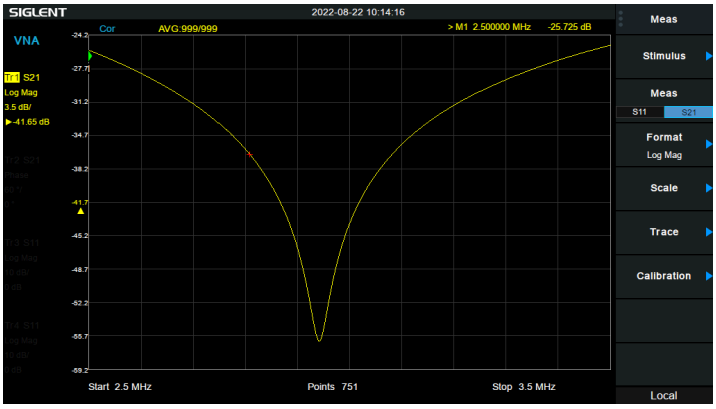

Figure 5.34: A screenshot of the 'Log Mag' format window showing the S21 parameter measurement in progress.

The reading for the impedance is collected using the 'Log Mag' format in 'dB', and the phase data is collected using the 'Phase' format in 'degree'. The $S21$ Log Mag data is in units of decibel and is converted to ohm using the following equation [33]:

$$S21[\Omega] = 10^{\frac{S21[\mathrm{dB}]}{20}}. \tag{5.2}$$

This data can now be fed into the following relation between the $S21$ parameter and the impedance Z, with $Z_{\mathrm{ref}} = 50\,\Omega$ for the SVA used here [34]

$$Z = 2 \cdot Z_{\mathrm{ref}} \cdot \left(\frac{1}{S21[\Omega]} - 1 \right). \tag{5.3}$$

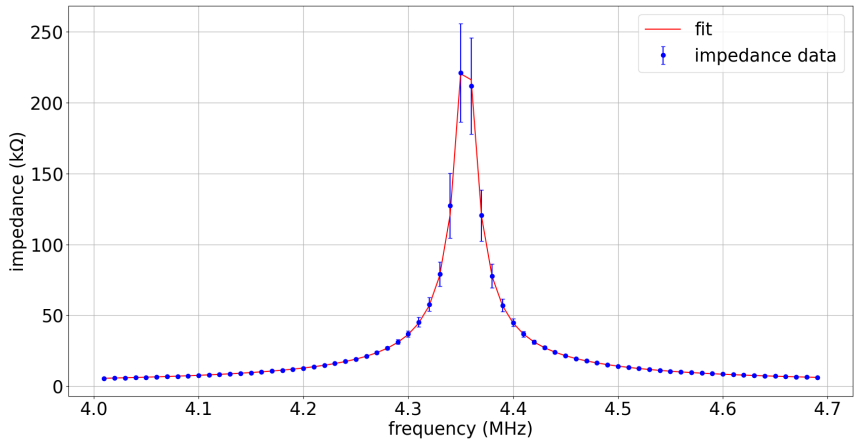

Figure 5.35: Impedance of the coil measured using the SVA.

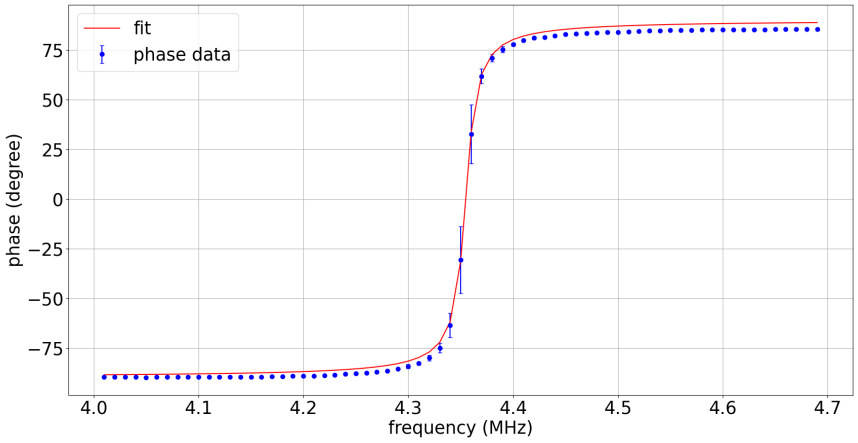

Figure 5.36: Phase readings corresponding to the impedance measurements from the previous plot.

The parameters are then obtained by fitting the data to the resonant function (see equation 6.2).

A striking difference between the two curves in Figure 5.30 and the curve from Figure 5.35 is the location of their resonance peaks. The resonant frequency F_r of an LCR circuit can be calculated using the following formula [35]:

$$F_r = \frac{1}{2\pi\sqrt{LC}}. \tag{5.4}$$

parameter	value
R [Ω]	3.383 ± 0.193
L [μH]	34.173 ± 0.332
C [pF]	39.086 ± 0.380

Table 5.2: Values of R, L and C parameters for the given coil setup.

Since the same coil is used in all these experiments, the L value can be assumed constant. The value of C will change depending on the setup being used. The only difference in the circuits used to collect data for Figure 5.30 is the pre-amplifier's presence or absence. The additional capacitance that the cable contributes, in addition to the capacitance of the coil, can explain the difference in the resonant frequencies. The pre-amplifier suppresses the capacitive influence of the cable, which is otherwise left unchecked in its absence.

Figure 5.37: An image of the LCR45 impedance and LCR meter.

Using an Atlas LCR45 handheld LCR meter [36], the cable's capacitance was determined to be $\sim 200\,\text{pF}$. A difference of 200 pF is sufficient to account for the resonant frequency difference between these two measurements (see section 5.2.4.4).

The difference in the resonant frequencies of the curves in Figure 5.30 and Figure 5.35 cannot be explained directly. The pre-amplifier is an active device; thus, the LCR45 cannot be used to determine its C value. However, the only logical explanation for this specific frequency difference is the capacitive influence of the pre-amplifier input.

CHAPTER

6

SIGNAL-TO-NOISE RATIO

6.1 Signal-to-Noise Ratio

Signal-to-Noise Ratio (SNR) is a dimensionless ratio of the powers of the signal and the noise. It is used to parameterize the performance of a device under test (DUT); the higher the ratio, the better the performance [37].

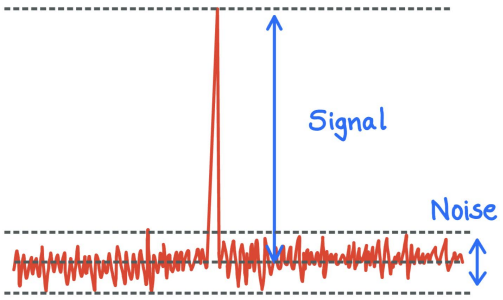

Figure 6.1: A general representation of a signal of interest and the accompanying noise.

The SNR is generally written as follows:

$$\mathrm{SNR} = \frac{U_{\mathrm{signal}}}{U_{\mathrm{noise}}}, \tag{6.1}$$

here U_{signal} is the signal, and U_{noise} is the noise.

6.2 Noise Model

In order to construct the SNR model, the coil's response to a beam current across the frequency range must be understood first. The resonant function of a given coil describes the behaviour of the coil across a frequency range and quantifies the behaviour at and around the resonant frequency. The resonant function of a Rogowski coil segment, with inductance L, capacitance C and resistance R, connected to a pre-amplifier with input resistance R_{out}, as a function of frequency ω, is given as

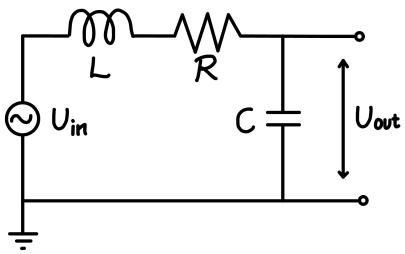

Figure 6.2: An equivalent circuit representing the coil segment.

$$F(\omega) = \frac{1}{\sqrt{\left(1-\omega^2 LC + \frac{R}{R_{\text{out}}}\right)^2 + \left(\frac{\omega L}{R_{\text{out}}} + \omega RC\right)^2}}. \tag{6.2}$$

From Table 5.2, we take R and L values, and the C value is calculated using equation 5.4. Plugging these values into equation 6.2, we get the following plot:

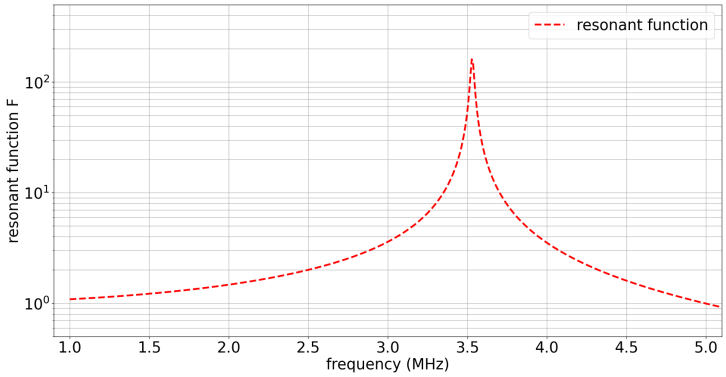

Figure 6.3: A plot of the frequency response function also called the Resonant function.

The magnetic flux Φ due to beam current I where R_t is the ratio of the small torus radius a_t to the large torus radius b_t at a point to the centre of the torus, is given by

$$\Phi = \mu_0 a_t n I \left(\frac{1-\sqrt{1-R_t^2}}{R_t}\right). \tag{6.3}$$

This magnetic flux induces a signal in the coil, which is subsequently read out through the pre-amplifier with gain g and is written as follows:

$$U(\omega) = g \cdot \omega \cdot F(\omega) \cdot \Phi. \tag{6.4}$$

The noise is modelled by adding the contributions from each component. The total noise contribution is given as follows:

$$U_{\text{total}}^{\text{noise}} = \sqrt{U_{\text{lock-in}}^{\text{noise}\ 2} + U_{\text{pre-amplifier}}^{\text{noise}\ 2} + g^2 \cdot U_{\text{coil}}^{\text{noise}2}}, \tag{6.5}$$

where

$$U_{\text{coil}}^{\text{noise}} = F(\omega) \cdot \sqrt{4k_B TR}. \tag{6.6}$$

Finally, the SNR is written by combining equations 6.4 and 6.5 as follows:

$$SNR = \frac{U(\omega)}{U_{\text{total}}^{\text{noise}}\sqrt{2\Delta f}}. \tag{6.7}$$

6.3 Signal and Noise Data

The noise profile has been measured in the previous chapter; the next step is to measure the coil's response to a current. The signal data will be used along with the noise data to calculate the SNR. The setup shown in Figure 6.4 is used for this experiment.

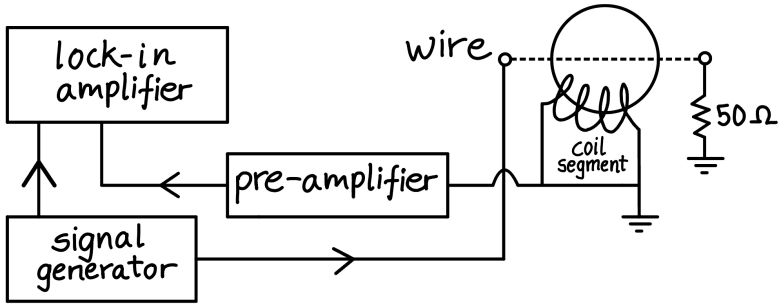

Figure 6.4: A schematic of the setup used for the signal response measurement.

The signal generator is programmed to send a sinusoidal wave of amplitude 10 mV_{pp} at a selected frequency. The lock-in amplifier is then set to sweep across ±10 kHz of the selected frequency; for example, if the signal generator sends a 1 MHz signal, the lock-in is set to sweep between 0.99 and 1.01 MHz. The signal from the coil segment via the pre-amplifier is then read out by the lock-in amplifier and saved. The amplitude value is then noted down for the selected frequency. This procedure is repeated for several points for all the coil segments.

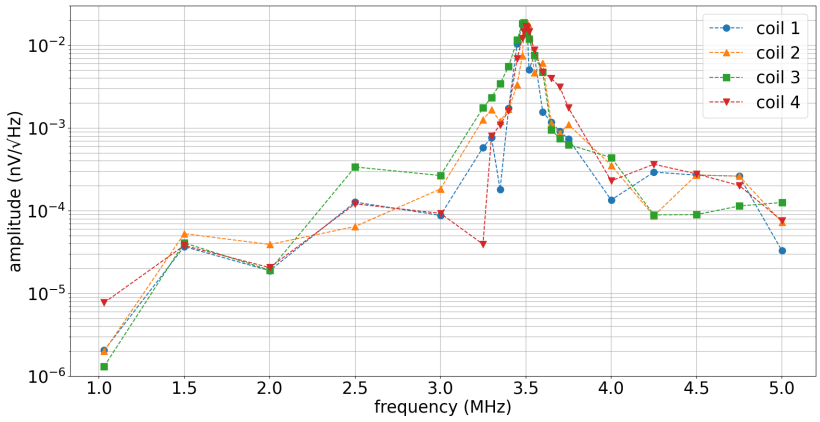

Figure 6.5: The signal response profile of the 4 coil segments.

Looking at Figure 6.5, it is visible that the coil segments show higher signal response at and around the resonant frequency. The curves have similar features for all four coil segments generally. Now the noise data is extracted from the results of section 5.2.4.4. This data is presented in Figure 6.6, where it is seen that the noise response is significantly smaller. Once again, all the coil segment noise responses have similar features.

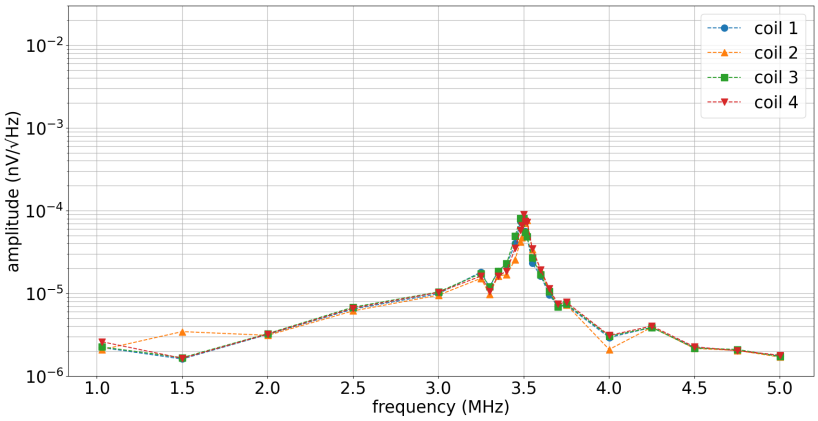

Figure 6.6: The noise response profile of the 4 coil segments.

6.4 Results

The SNR can now be calculated using the data from Figure 6.5 and Figure 6.6 for the individual coil segments. In the SNR model, $a_t = 6.08 \times 10^{-3}$ m, $b_t = 58.32 \times 10^{-3}$ m and $I = 70.7\,\mu$A.

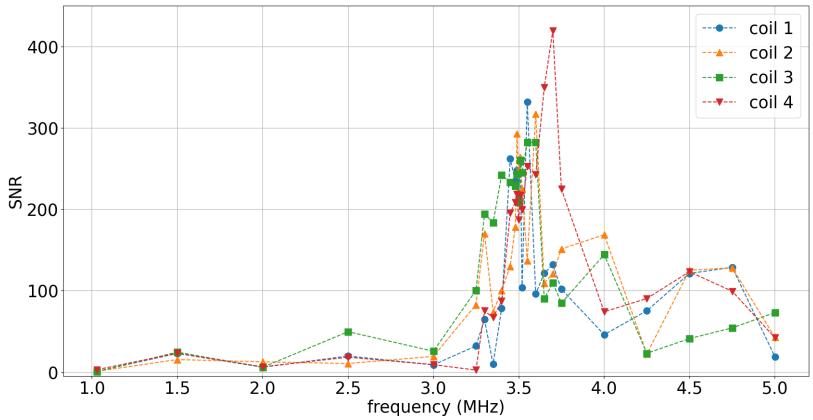

Figure 6.7: SNR of the 4 coils as a function of frequency.

From Figure 6.7, it is apparent that the coil segments have similar SNR profiles as expected. These SNR data points can be combined to produce a general SNR profile for the setup. The top plot in Figure 6.8 is a combined SNR profile of the Rogowski BPM setup. The bottom plot is obtained using the SNR model mentioned in section 6.2 of this chapter.

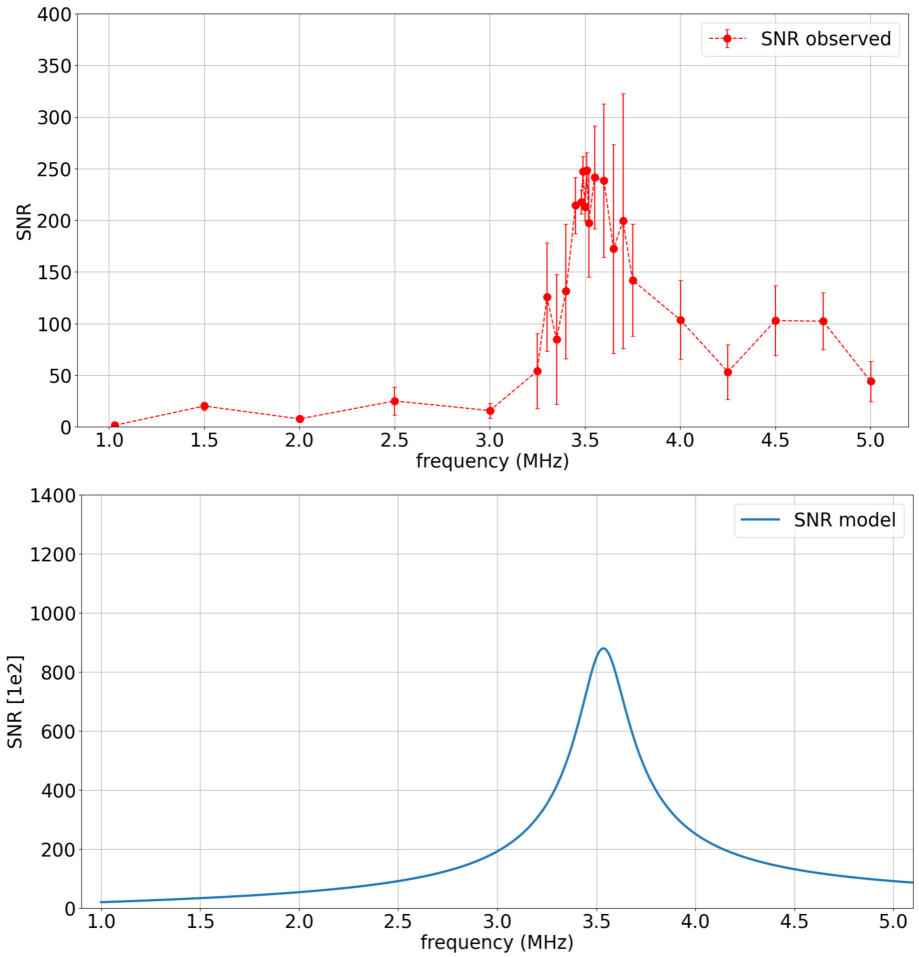

Figure 6.8: Comparing SNR observed (top, averaged data with RMS error) and SNR model (bottom).

The observed and predicted/model values have an almost constant discrepancy throughout the frequency range in Figure 6.8. An impedance mismatch at the coil segment - pre-amplifier junction can be the reason for this discrepancy, which can be mitigated by designing pre-amplifiers compatible with the Rogowski BPMs. It is observed that the SNR is best at and around the resonant frequency. The plots from the SNR model and the experimental results have a similar profile over the frequency range. The experiment data has a maximum SNR of ~ 250 at the resonance peak.

CHAPTER

7

CONCLUSION & OUTLOOK

High-precision EDM measurements require high-quality beams, which cannot be delivered without deploying high-precision BPMs. The Rogowski BPM is a perfect fit for this role, not only because of its good resolution and performance but also for being cost-effective and compact.

In this thesis, the SNR of the Rogowski BPM was studied, showing promising results. When operated inside the resonance range, the setup is highly efficient, with a SNR of almost 250. The coil segments can be tuned to the required frequency range (either while production or tuning capacitors). Therefore the SNR can be optimized based on the use case by aligning the BPM resonant frequency to the operating frequency of the beam.

Compared to other beam position monitoring systems, the Rogowski BPMs have several advantages, as stated earlier. A significant improvement in the SNR can be expected with a few minor updates to the current system, such as a purpose-built pre-amplifier.

LIST OF FIGURES

BIBLIOGRAPHY

[1] P. Rodgers, "Where did all the antimatter go?," *Physics World*, vol. 14, p. 11, Aug 2001.

[2] L. Canetti, M. Drewes, and M. Shaposhnikov, "Matter and Antimatter in the Universe," *New Journal of Physics*, vol. 14, no. 9, p. 095012, 2012.

[3] W. Bernreuther, "CP violation and baryogenesis," *CP Violation in Particle, Nuclear and Astrophysics*, pp. 237–293, 2002.

[4] A. D. Sakharov, "Violation of CP-invariance, C-asymmetry, and baryon asymmetry of the Universe," *In The Intermissions... Collected Works on Research into the Essentials of Theoretical Physics in Russian Federal Nuclear Center, Arzamas-16*, pp. 84–87, 1998.

[5] J. Pretz, "Polarization measurements for Electric Dipole Moment and Axion/ALP searches," *PhD School & Workshop Aspects of Symmetries*, Nov 2021.

[6] F. Rathmann, A. Saleev, and N. Nikolaev, "The search for electric dipole moments of light ions in storage rings," *Journal of Physics: Conference Series*, vol. 447, p. 012011, Jul 2013.

[7] V. Bargmann, L. Michel, and V. Telegdi, "Precession of the polarization of particles moving in a homogeneous electromagnetic field," *Physical Review Letters*, vol. 2, no. 10, p. 435, 1959.

[8] H. Stein, D. Prasuhn, H. Stockhorst, J. Dietrich, K. Phan, V. Kamerdzhiev, R. Maier, I. Meshkov, A. Sidorin, and V. Parkhomchuk,

"Current status of the COSY electron cooler (Jülich, Germany)," *Atomic energy*, vol. 94, no. 1, pp. 24–26, 2003.

[9] T. Wagner, *Beam-based alignment at the Cooler Synchrotron COSY for an Electric Dipole Moment measurement of charged particles*. PhD thesis, RWTH Aachen University, 2021.

[10] P. Forck, D. Liakin, and P. Kowina, "Beam position monitors," *CERN*, 2009.

[11] R. Suvarna, "Rogowski Beam Position Monitor," *Workshop on Polarized Sources Targets and Polarimetry 2022 (PSTP22)*, Sep 2022.

[12] V. Kamerdzhiev, I. Bekman, C. Böhme, B. Lorentz, S. Merzliakov, P. Niedermayer, K. Reimers, M. Simon, and M. Thelen, "BPM System Upgrade at COSY," *7th International Beam Instrumentation Conference (IBIC2018)*, Jul 2018.

[13] J. D. Ramboz, "Machinable Rogowski coil, design, and calibration," *IEEE Transactions on Instrumentation and measurement*, vol. 45, no. 2, pp. 511–515, 1996.

[14] D. J. Griffiths, *Introduction to Electrodynamics*. Cambridge University Press, 4 ed., 2017.

[15] S. Hacıömeroğlu, D. Kawall, Y.-H. Lee, A. Matlashov, Z. Omarov, and Y. K. Semertzidis, "SQUID-based beam position monitor," *The 39th International Conference on High Energy Physics (ICHEP2018)*, vol. 4, no. 11, 2018.

[16] F. Rathmann, "First direct hadron EDM measurement with deuterons using COSY," *Willy Haeberli Memorial Symposium*, Jun 2022.

[17] R. Geithner, R. Neubert, W. Vodel, M. Schwickert, H. Reeg, R. von Hahn, and P. Seidel, "A non-destructive beam monitoring system based on an LTS-SQUID," *IEEE transactions on applied superconductivity*, vol. 21, no. 3, pp. 444–447, 2010.

[18] J. B. Johnson, "Thermal agitation of electricity in conductors," *Physical review*, vol. 32, no. 1, p. 97, 1928.

[19] W. Schottky, "On spontaneous current fluctuations in various electrical conductors," *Journal of Micro/Nanolithography, MEMS, and MOEMS*, vol. 17, no. 4, p. 041001, 2018.

[20] F. Fouquet, *Noise in Radio-frequency Electronics and Its Measurement*. John Wiley & Sons, 2020.

[21] M. Alem, "Noise Spectral Density Measured with Lock-in Amplifiers," *Zurich Instruments*, Aug 2021.

[22] J. G. Proakis and M. Salehi, *Digital communications*. McGraw-Hill, 2007.

[23] "HF2 User Manual," *Zurich Instruments*, Aug 2022.

[24] "LabOne Programming Manual," *Zurich Instruments*, Aug 2022.

[25] G. Torzo and G. Delfitto, "The lock-in amplifier: what is it for? how to build one?," *Revista Brasileira de Ensino de Física*, vol. 44, 2022.

[26] W. Yu, "How to Check the Input Noise Level of the MFLI," *Zurich Instruments*, Dec 2020.

[27] "NEK Sealine RG 58 C/U Marine Cable Datasheet," *NEK Kabel AS*.

[28] "About Lock-In Amplifiers (Application Note #3)," *Stanford Research Systems*.

[29] S. Merzliakov, C. Böhme, and V. Kamerdzhiev, "Low-Noise BPM Preamplier for the HESR," *Jahresbericht 2016 Einzelbeiträge*, pp. 36–37, 2016.

[30] F. Abusaif, *Development of compact, highly sensitive beam position monitors for storage rings*. PhD thesis, RWTH Aachen University, 2021.

[31] B. Whitlock, "Understanding, finding, & eliminating ground loops," *Handout for Courses A14T and B50T, CEDIA*, p. 108, 2003.

[32] "SVA1000X Series Spectrum Analyzer User Manual," *Siglent Technologies*, Jun 2018.

[33] R. Richards, "EMC Related Formulae," *Toprudder EMC*, Mar 2003.

[34] S. M. Sandler, "Extending the Usable Range of the 2-Port Shunt Through Impedance Measurement," *IEEE MTT-S Latin America Microwave Conference (LAMC-2016)*, pp. 1–3, 2016.

[35] Y. Kraftmakher, "Demonstrations with an LCR Circuit," *The Physics Teacher*, vol. 49, no. 3, pp. 168–170, 2011.

[36] "Passive Component Impedance Meter Model LCR45 Datasheet," *Peak Electronic Design Limited*, Dec 2013.

[37] D. H. Johnson, "Signal-to-Noise Ratio," *Scholarpedia*, vol. 1, no. 12, p. 2088, 2006.